

Inferences on the mantle viscosity structure and the post-overturn evolutionary state of Venus

T. Rolf^{a,*}, B. Steinberger^{b,a}, U. Sruthi^a, S. C. Werner^a

^a*Centre for Earth Evolution and Dynamics, University of Oslo, 0315 Oslo, Norway*

^b*GFZ German Research Centre for Geosciences, Telegrafenberg, 14473 Potsdam, Germany*

Abstract

Venus has similar size, density and bulk composition as Earth, but has tectonically evolved clearly differently, and this divergence remains enigmatic. Surface observations such as gravity, topography and surface age constrain Venus' evolution, but interpreting these signals requires understanding of the surface-interior coupling and thus insight into the structure and evolution of the venusian mantle and lithosphere. Here, we investigate how such observables may be generated from interior dynamics using numerical forward models of global mantle convection that consistently link the thermochemical, magmatic and tectonic evolution of Venus. Venus' present surface gravity spectrum and its relation to topography is matched best by our models with a mantle viscosity profile featuring a sublithospheric minimum of $\sim 2 \times 10^{20}$ Pa s and a gradual increase by a factor of ~ 100 down to a depth of ~ 250 km above the core-mantle boundary. No pronounced viscosity jump around the mantle transition as inferred for Earth is favoured for Venus, which points to a relatively dry venusian upper mantle compared to Earth's as previously suggested. This holds true for both a pure stagnant-lid scenario and in the presence of episodic catastrophic overturns triggered by cumulative crustal growth due to on-going magmatism and volcanism. Overturns strongly perturb the surface gravity spectrum up to ~ 150 Myr after overturn cessation. Material deeply recycled by the resurfacing event annihilates the developed plume pattern, which needs much longer than those 150 Myr to recover to a state comparable to the pattern suggested by thermal emissivity anomalies observed on Venus. Moreover, overturns limit crustal thicknesses to reasonable values and are more capable than stagnant-lid evolutions in generating mean surface ages > 500 Myr. These findings seem to confirm previous suggestions that the episodic regime is more applicable to Venus than a purely stagnant-lid regime. Yet, the relatively long time span required to recycle the entire surface ($\sim 150 - 200$ Myr) and the presently on-going volcanic resurfacing predicted by our models complicate the formation of a uniform surface age as indicated by Venus' crater population and may also suggest that the latest

*Corresponding author

Email address: tobias.rolf@geo.uio.no (T. Rolf)

overturn has ceased longer ago than indicated by Venus' present mean surface age.

Keywords: Venus, Mantle evolution, Gravity Spectrum, Viscosity structure

1. Introduction

Venus is regularly called Earth's "sister planet", but clearly the evolutions of both planets have diverged at some point. This is ultimately expressed by the current operation of plate tectonics on Earth, but not on Venus. The absence of continuous plate tectonic recycling on Venus may explain several first-order observations made about our closest planetary neighbour, such as the dearth of an internally generated magnetic field and the presence of a dense, dry CO₂-rich atmosphere (e.g. Driscoll and Bercovici, 2013; Gillmann and Tackley, 2014). The reason for the tectonic discrepancy of the two bodies has remained an enigma in planetary dynamics for many years. Possible explanations range from Venus' much higher surface temperature, which enhances healing of tectonic damage and thus complicates the development of tectonic plates (e.g. Bercovici and Ricard, 2014), to a lower water content of the venusian interior, to bi-stable planetary evolutions, in which multiple tectonic regimes would be equally feasible over a range of plausible conditions (e.g. Weller et al., 2015). In the latter case, stochastic perturbations, for instance early asteroidal impacts (see e.g. O'Neill et al., 2017) may be sufficient to change the tectonic evolution scenario.

Most suggestions demonstrate the importance of the coupling between surface and interior. For instance, melting and outgassing of Venus' interior may have caused its dehydration and the development of thick atmosphere as well as high surface temperature, which then prevented sufficient long-term damage of Venus' surface rocks to establish an Earth-like crustal recycling mechanism. On Earth, the surface plates are mostly an expression of large-scale convection in the deep interior (Bercovici, 2003), but Venus' surface lacks continuously mobile and subducting plates. As such, surface-interior coupling may function differently. Yet, the details of such a presumed coupling remain insufficiently understood.

Understanding these issues requires advanced insights into (1) Venus' present interior state in comparison to Earth's and (2) the planet's evolutionary path given the absence of clear features related to plate recycling. Concerning (1), direct observations of Venus' interior are essentially not available due to the lack of seismic measurements, so that inferences on the deep interior can only be drawn indirectly, for example by interpreting surface signals such as gravity and topography. At least at long-wavelength, these signals are linked to the structure and dynamics of the sublithospheric mantle (Pauer et al., 2006; Steinberger et al., 2010), but gravity interpretation is usually non-unique (see e.g. Wiczorek, 2007) and has to be embedded into (2) a consistent context of Venus' evolution.

Currently, Venus may be in the stagnant-lid mode of convection (see e.g.

40 Solomatov, 1995) in which the shallow lithosphere can uplift and subside (dy-
41 namic topography), but is not substantially weakened and structured by tec-
42 tonic forces arising from deep mantle flow compared to Earth. Subduction-like
43 processes on Venus have been proposed though (Schubert and Sandwell, 1995),
44 perhaps triggered by mantle plumes (Davaille et al., 2017), so that Venus may
45 be in a transitional regime between an Earth-like continuously mobilised litho-
46 sphere and a more conventional stagnant-lid, such as contemporary Mars or
47 Mercury.

48 This transitional regime may be characterised by episodic mobile-lid be-
49 haviour during earlier phases of Venus’ evolution. The observed, roughly ran-
50 dom, distribution of impact craters on Venus (Herrick, 1994) in fact suggests
51 a rather young (750^{+250}_{-450} Myr, McKinnon et al., 1997) and essentially uniform
52 surface age, which favours a global event of surface mobilisation and tectonic
53 resurfacing around that time (e.g. Romeo and Turcotte, 2010). Nonetheless,
54 crater statistics have large uncertainties and the comparably small number of
55 craters on Venus also strongly limits the length scales over which inferences can
56 be made, so that the possibility of equilibrium resurfacing such as by volcanism,
57 cannot be rejected per se (e.g. Bjonnes et al., 2012). A hybrid mode in which
58 episodic tectonic recycling cools the interior and subsequently reduces the in-
59 tensity of the (still on-going) volcanic resurfacing may provide the most feasible
60 scenario. We come back to this in section 3.3.

61 The uncertainties about the style and evolution of Venus’ convective regime
62 complicate the interpretation of present-day observables. In particular, it is not
63 sufficiently understood how such observables may depend on Venus’ convective
64 regime; specifically, how they would respond to episodes of surface mobilisation
65 and tectonic recycling. If the aftermath of a global overturn lasts short compared
66 to Venus’ characteristic surface age, then present Venus may be representative of
67 the stagnant-lid mode. But if remnants of the latest overturn episode can persist
68 sufficiently long in Venus’ interior, this could affect the present flow pattern and
69 structure in the mantle, which could be reflected in present surface observables
70 such as topography and gravity. Yet, the aftermath of a global overturn and its
71 thermochemical and magmatic consequences remain insufficiently understood.

72 To gain deeper insight into these aspects, it is necessary to decipher the
73 relation between deep mantle structure and dynamics as well as surface observ-
74 ables in a consistent evolutionary framework. Here, we use a numerical model of
75 Venus’ interior that links together the thermochemical, magmatic and tectonic
76 evolution of the planet. We employ this framework in order to (1) constrain a
77 likely present-day structure of Venus’ mantle focussing on mantle viscosity and
78 (2) to make inferences on the evolutionary state on Venus in relation to the
79 proposed global resurfacing events.

80 **2. Methodology**

81 *2.1. Numerical model*

82 We compute the thermochemical evolution of Venus’ interior using the man-
83 tle convection code StagYY (Tackley, 2008). Our setup is similar to the one

84 used in Armann and Tackley (2012), where additional model details can be
 85 found. A major difference is that we use a 3D spherical rather than 2D annulus
 86 geometry. On the other hand our incorporation of mineral physics is simpler
 87 in the sense that we assume the venusian mantle to be incompressible. Specifi-
 88 cally, we employ the extended Boussinesq approximation in which the terms for
 89 viscous dissipation and adiabatic heating are included in the energy equation,
 90 which makes it more consistent with regards to latent heat effects, such as those
 91 related to the presence of phase transitions (see Christensen and Yuen, 1985).
 92 Consequently, our models include an adiabatic temperature increase across the
 93 entire mantle of ~ 850 K.

94 Since our model assumes that the mantle is an incompressible fluid, den-
 95 sity cannot explicitly depend on depth in the extended Boussinesq limit, but
 96 other thermodynamic parameters could. This concerns mainly thermal expan-
 97 sivity, but also thermal conductivity and the gravitational acceleration. We do
 98 not consider variations of these parameters due to temperature and/or pressure
 99 variations (see discussion in section 4) as this strategy allows us to compare our
 100 results more directly to those of Huang et al. (2013). These authors also em-
 101 ployed the extended Boussinesq limit without depth variation of thermodynami-
 102 cal parameters and gravity; but their treatment neglected overturn scenarios like
 103 the ones considered here. In contrast, Armann and Tackley (2012) employed a
 104 2D compressible, anelastic model including radial variation of thermodynamical
 105 parameters (not gravity) and also considered overturn episodes. Yet, our study
 106 discusses several diagnostics with inherent 3D nature (see section 2.3), such as
 107 the planetary gravity spectrum, the spatial pattern of mantle plumes and the
 108 modes of crustal recycling that impact the surface age distribution. As a con-
 109 sequence, we preferred using 3D models for the sake of better comparability to
 110 observations; the cost of this is a somewhat reduced complexity of our physical
 111 model compared to the one of Armann and Tackley (2012).

112 The model domain is a 3D spherical shell with core radius R_C and surface
 113 radius R_S , which has free-slip mechanical boundary conditions at both bound-
 114 aries. The shell is discretised on a YinYang grid whose two grid blocks have
 115 a resolution of $64 \times 192 \times 64$ cells each. The radial grid spacing is refined to
 116 $\sim 20 - 25$ km close to the surface, near the phase changes in the transition zone
 117 and at the core-mantle boundary. The shell is cooled from above ($T = T_S$)
 118 and heated from below ($T = T_C(t)$) as well as from within using a generic bulk
 119 heating rate of $H(t) = H_P \exp(t/\tau \ln 2)$.

120 In most model cases, we chose the present-day value $H_P = H(t = 0 \text{ Ga}) =$
 121 $5 \times 10^{-12} \text{ W kg}^{-1}$, but in two cases we used reduced values to test the effect of
 122 this parameter. Our nominal value of H_P is comparable to, but at the lower
 123 end of the range inferred for present-day Earth (see e.g. Turcotte and Schubert,
 124 2002). We employed a decay constant of $\tau = 3 \text{ Gyr}$, such that the internal
 125 heating rate at model initiation ($t = t_0 = 4.4 \text{ Ga}$) is about $2.8\times$ higher than at
 126 present day. Radiogenic decay is thus somewhat less pronounced than during
 127 Earth's, and Venus' history, implying that our models may feature somewhat
 128 less radiogenic heating during the earlier stages of evolution. While this is to be
 129 improved in future models, we made this choice to limit the vigour of convection

130 and the degree of partial melting (see below), which require extra treatment and
131 would significantly increase computational costs. Our present study is mostly
132 concerned about present-day observables and Venus’ late-stage history, but we
133 note that inheritance from earlier periods could play a role in some aspects.

134 Besides its overall amount, internal heat is generated uniformly across the
135 mantle except in two cases where it is more enriched by a factor ΔH in the
136 basaltic material that typically represents the crust (see below). Surface tem-
137 perature is constant through time (cf. Gillmann and Tackley, 2014), but core-
138 mantle boundary (CMB) temperature T_C evolves in time from its initial value
139 T_{c0} in response to the heat flow Q_C across the CMB as $dT_C/dt = -Q_C/M_C c_{p,C}$,
140 where M_C is the core mass and $c_{p,C}$ is the core’s specific heat capacity. This
141 simple core model does not consider the possibility of internal heat generation
142 in the core or other complexities like inner core crystallisation. However, our
143 knowledge of Venus’ core is very fragmentary so that a more sophisticated ap-
144 proach would lack sufficient ground truth.

145 *2.1.1. Composition and mineralogy*

146 Material composition is tracked by 1.44×10^8 tracer particles using the tracer-
147 ratio method (Tackley and King, 2003). This corresponds to an average of ~ 90
148 tracers per grid cell. The tracers are used to map composition into a continuous
149 field ($0 \leq C \leq 1$) that represents a mixture of two end-member components:
150 basalt ($C = 1$) and harzburgite ($C = 0$). Basalt is assumed to consist of 100%
151 pyroxene-garnet, while harzburgite is composed of 25% pyroxene-garnet and
152 75% olivine (see Xie and Tackley, 2004).

153 Initially, the described mixture is homogeneous in the entire model (see sec-
154 tion 2.2), but it evolves with time depending on the thermal and magmatic
155 history of the material: if the temperature of a patch exceeds its solidus, its
156 basaltic components can partially melt and composition changes. The solidus
157 is here given by a fit to experimental data on Earth’s mantle rocks (see Xie and
158 Tackley, 2004). Upon melting, latent heat is consumed. In the upper mantle,
159 melt is assumed to be buoyant and to rise quickly. This process is simplified
160 here by an immediate extraction of melt from the mantle; the extracted ma-
161 terial is emplaced at the surface as basaltic crust. The residue is depleted in
162 basalt and becomes more difficult to melt: the solidus increases linearly with
163 decreasing basalt content (by up to 150 K when the basalt fraction approaches
164 0%). Generally, melt extraction is limited to the upper mantle here, that is
165 above 730 km.

166 Some major phase transitions are included in our model, as they may be im-
167 portant for generating mantle flow patterns consistent with Venus’ geoid (Huang
168 et al., 2013). These transitions happen at somewhat greater depth than on
169 Earth due to the lower venusian gravity. The olivine and the pyroxene-garnet
170 system have distinct phase transitions (see Xie and Tackley, 2004; Armann and
171 Tackley, 2012, for details). Specifically, olivine converts into magnesiowüstite
172 at $d = 450$ km and further into perovskite at $d = 730$ km depth. The pyroxene-
173 garnet system considers three transitions at depths of 65, 440, and 800 km the
174 first of which describes the transition from basalt to eclogite. The assumed prop-

Symbol	Definition	Value
R_S	Planetary mean radius	6052 km
R_C	Core radius	3186 km
D_0	Mantle thickness	2866 km
g_0	Gravitational acceleration	8.87 m s^{-2}
T_S	Surface temperature	740 K
T_{C0}	Initial CMB temperature	3850 K
ΔT	Superadiabatic temperature drop	2300 K
H_P	Present-day bulk internal heating rate	$5 \times 10^{-12} \text{ W kg}^{-1}$
τ	Radiogenic decay constant	$3.0 \times 10^9 \text{ yr}$
ρ_0	Mantle density	3378 kg m^{-3}
k_0	Mantle thermal conductivity	$4 \text{ W m}^{-1} \text{ K}^{-1}$
c_{p0}	Mantle specific heat capacity	$1250 \text{ J kg}^{-1} \text{ K}^{-1}$
$c_{p,C}$	Core specific heat capacity	$800 \text{ J kg}^{-1} \text{ K}^{-1}$
α_0	Mantle thermal expansivity	$2 \times 10^{-5} \text{ K}^{-1}$
E_A	Activation energy	$2 \times 10^5 \text{ J mol}^{-1}$
μ	Friction coefficient	0.5
L_m	Latent heat of melting	$6 \times 10^5 \text{ J kg}^{-1}$
$\Delta\rho_S$	Surface density jump	3318 kg m^{-3}
$\Delta\rho_C$	CMB density jump	4357 kg m^{-3}
$\Delta\rho_{ol_{450/730}}$	Density jumps (ol)	$250/150 \text{ kg m}^{-3}$
$\Delta\rho_{px_{65/440/800}}$	Density jumps (px)	$250/150/150 \text{ kg m}^{-3}$
$\gamma_{ol_{450/730}}$	Clapeyron slopes (ol)	$2/ - 2 \text{ MPa K}^{-1}$
$\gamma_{px_{65/440/800}}$	Clapeyron slopes (px)	$0/1/1 \text{ MPa K}^{-1}$

Table 1: Symbols, definitions and reference values used in this study. The last four rows contain multiple values that describe the respective values for the different phase transitions: either 2 in the olivine (ol) system or 3 in the pyroxene-garnet (px) system. The numeric subscripts in these variable names denote the depth of the phase transitions in kilometres.

175 erities of all phase transitions, such as Clapeyron slopes and density increases,
176 are kept fixed here and are summarised in Table 1.

177 2.1.2. Viscosity calculation

178 In this section, we describe how our model computes an effective material
179 viscosity. In summary, effective viscosity η is computed as the harmonic average
180 of two contributions of which the first one, η_1 , is described by an Arrhenius law

$$\eta_1 = A\eta_p \exp\left(\frac{E_A + pV_A}{R_g T}\right), \quad (1)$$

181 where $A = A(\eta_0)$ is a pre-factor that forces η_1 to be equal to the reference
182 viscosity η_0 at temperature $T = 1613 \text{ K}$ and pressure $p = 0 \text{ Pa}$. The term
183 η_p describes the phase dependence. For simplicity, we only consider a vis-
184 cosity increase across the transition to perovskite, that is the lower mantle
185 phase in which $\eta_p = \Delta\eta_p$, so that $\eta_p = 1$ elsewhere. By convention, R_g is

186 the gas constant and V_A the activation volume, which depends on pressure as
 187 $V_A(p) = V_{A0} \exp(-p/p^*)$ (Tackley et al., 2013). Here, we use $p^* = 400$ GPa
 188 to account for the reduction of activation volume in the lowermost mantle and
 189 V_{A0} is the activation volume at $p = 0$ Pa. We assign the activation energy E_A
 190 a moderate value of 200 kJ mol^{-1} as a compromise between realism and numer-
 191 ical feasibility. However, the chosen value is large enough to allow for strong
 192 thermal viscosity variation and thus for the formation of a stagnant lid on top
 193 of the convecting mantle (see Solomatov, 1995). For simplicity, viscosity does
 194 not explicitly depend on composition and the rheological parameters except η_p
 195 are independent of phase (see Table 1). For numerical reasons, the range over
 196 which viscosity can vary is limited to the interval $[10^{18}, 10^{25}]$ Pa s.

197 In the stagnant-lid set of calculations (described below), effective viscosity is
 198 completely determined by η_1 . In some cases we employ a viscoplastic rheology
 199 to allow the lithosphere to fail plastically when the convective stresses reach
 200 the yield stress σ_Y . The yield stress is depth-dependent based on Byerlee’s law
 201 using a friction coefficient of $\mu = 0.5$ (and a cohesion of 0 Pa), but is bounded
 202 by a maximum value σ_0 , thus,

$$\sigma_Y = \min(\mu p, \sigma_0). \quad (2)$$

203 In case of plastic yielding, the viscosity is reduced to $\eta_2 = \sigma_Y/2\dot{\epsilon}$, where $\dot{\epsilon}$ is the
 204 2nd invariant of the strain rate tensor, and the effective viscosity is then given by
 205 $\eta = (1/\eta_1 + 1/\eta_2)^{-1}$. This method has turned out to be a viable parametrisation
 206 to generate large-scale lithospheric overturn events that may have occurred
 207 during Venus’ evolution (e.g. Moresi and Solomatov, 1998; Armann and Tackley,
 208 2012).

209 2.2. Computed evolutions

210 We compute Venus’ mantle evolution from $t_0 = 4.4$ Ga until present-day as
 211 described above. We chose this rather late initiation time t_0 , because we assume
 212 a solid-state interior in our model that does not properly capture the dynamics of
 213 a largely molten mantle during the initial stages of planetary thermal evolution.
 214 In all cases, we use the same initial condition in which temperature increases
 215 from its fixed surface value across an 80 km thick boundary layer to an internal
 216 temperature of ~ 1900 K, which assumes that mantle temperature was higher
 217 early in planetary evolution than at present (see e.g. Herzberg et al., 2010).
 218 Below the boundary layer, temperature increases adiabatically until the bottom
 219 boundary layer is reached. At this point, temperature increases strongly to the
 220 initial CMB value. The entire mantle is initialized with a bulk composition of
 221 $C = 0.2$, that is 80% harzburgite and 20% basalt and consequently a mix of
 222 60% olivine and 40% pyroxene (see section 2.1.1).

223 We compute two sets of evolutions. In the first set, the stagnant-lid (S)-
 224 family, we compute 10 evolutions in which plastic failure of the lithosphere is
 225 inhibited. In these cases, we focus on the role of the rheological parameters
 226 η_0 , V_{A0} , and $\Delta\eta_p$ in the evolution of venusian mantle dynamics and its surface
 227 expressions. After defining a preferred case, we use the rheological parameters of

Case	η_0	V_{A0}	$\Delta\eta_p$	σ_0	H_P	ΔH
S1	0.3	3.5	1	–	5	1
S2	1	3.5	1	–	5	1
S2a	1	3.5	1	–	4	1
S2b	1	3.5	1	–	5	10
S3	3	3.5	1	–	5	1
S4	10	3.5	1	–	5	1
S5	1	2.5	1	–	5	1
S6	1	4.5	1	–	5	1
S7	1	3.5	5	–	5	1
S8	1	3.5	20	–	5	1
E30	1	3.5	1	30	5	1
E50	1	3.5	1	50	5	1
E50a	1	3.5	1	50	4	1
E50b	1	3.5	1	50	5	10
E55	1	3.5	1	55	5	1
E60	1	3.5	1	60	5	1
E70	1	3.5	1	70	5	1

Table 2: List of performed calculations and their characterising parameters, η_0 , V_{A0} , $\Delta\eta_p$, σ_0 , H_P , and ΔH . Values of η_0 are scaled with a value of 10^{21} Pa.s, values of V_{A0} are given in $10^{-6}\text{m}^3\text{mol}^{-1}$ and those for H_P in 10^{-12}Wkg^{-1} . Stagnant cases (S) do not consider a yield stress, while episodic cases (E) feature finite values, given in MPa. In the latter set, the numeric part of the case name denotes the value of σ_0 in MPa.

228 this case to compute a second set of 7 calculations in which episodic lithospheric
229 failure is allowed for (dubbed the E-family). In this set, we mostly focus on
230 variation of the yield stress, which determines how easily the lithosphere can
231 fail. An overview of the computed cases and their characterising parameters is
232 given in Table 2.

233 2.3. Diagnostics

234 For all cases, we compute a number of diagnostics and the resulting values are
235 summarised in Table 3. In particular, we compute the average heat flux across
236 the surface (q_S) and CMB (q_C) at present-day, which are given by Fourier’s
237 law $\overline{q_{S,C}} = -k_{S,C} \partial T / \partial r$. In addition, we compute the number of hot mantle
238 plumes (described in section 3.1.3) and crustal thickness (see section 3.3.1).
239 Primarily though, we compute the surface geoid under self-gravitation following
240 the approach described in Zhong et al. (2008), which is based on Zhang and
241 Christensen (1993). We describe this approach only conceptually here, for a
242 more detailed description including equations we refer to these papers. We
243 first use the thermochemical density heterogeneities arising from integrating
244 the evolution equations (Stokes flow) forward in time and convert them into
245 spectral space ($\delta\rho_{lm}$), where l and m are degree and order of the spherical
246 harmonic, respectively. Such density anomalies drive the large-scale convective
247 flow and thus lead to deflection of the surface and CMB (Hager et al., 1985);

248 these define the dynamic topography.

249 With the free-slip boundary conditions in our model, these deflections are
 250 estimated from the respective normal stress acting on these boundaries as well as
 251 the density jumps $\Delta\rho_s$ and $\Delta\rho_c$ across these boundaries, and are also converted
 252 into spectral space (δs_{lm} and δc_{lm}). With $\delta\rho_{lm}$, δs_{lm} and δc_{lm} the gravitational
 253 potential at the surface (Φ_{lm}) and CMB (Ψ_{lm}) can in principle be estimated, but
 254 both δs_{lm} and δc_{lm} depend in turn on these potentials. In the spectral domain
 255 it is possible though to couple the expressions and solve for Φ_{lm} , Ψ_{lm} , δs_{lm}
 256 and δc_{lm} simultaneously for a given combination of l and m (see e.g. Appendix
 257 A in Zhong et al., 2008). The same method has already been used in StagYY
 258 models of Venus’ interior by Armann and Tackley (2012), but their 2D spherical
 259 annulus models could only capture sectoral harmonics (i.e., $l = m$), so that not
 260 the entire spectrum was included in their analysis.

261 Once Φ_{lm} has been computed in the spectral domain (we do not further
 262 discuss Ψ_{lm} here), it is straightforward to synthesise it into its power spectrum
 263 P_{gg} . Following Steinberger and Holme (2002), we define the dimensionless power
 264 spectrum as

$$P_{gg}(l) = (l + 1) \left(g_{l0}^2 + \sum_{m=1}^l g_{lm}^2 + h_{lm}^2 \right), \quad (3)$$

265 where g_{lm} and h_{lm} are the fully normalised spherical harmonic expansion coef-
 266 ficients of the gravitational potential. Here, we only consider the degree range
 267 of spherical harmonics as $2 \leq l \leq 16 = l_{max}$ ($m \leq l$). In this range, P_{gg} is
 268 likely predominantly generated by deep (mantle) rather than shallow (crustal)
 269 sources and can thus be used to make inferences on the structure of the deep
 270 interior at this range of spatial wavelengths (Steinberger et al., 2010). In an
 271 analogous way, we can define the power spectrum of surface topography P_{tt}
 272 and the cross-power spectrum P_{gt} , which we use to build the degree correlation
 273 $C_{gt}(l) = P_{gt}/\sqrt{P_{gg}P_{tt}}$ and the spectral ratio $R_{gt}(l) = \sqrt{P_{gg}/P_{tt}}$ of gravity and
 274 topography.

275 Our approach assumes a purely viscous body and does not involve elastic
 276 effects within the lithosphere (e.g. Turcotte et al., 1981). These change the dis-
 277 placement of the surface (i.e. topography) upon loading and consequently the
 278 gravity signal, in particular when lithospheric thickness is large. For internal
 279 loads that are most relevant for the present study, however, Steinberger et al.
 280 (2015) suggest that the resulting reduction in topography may not be as large
 281 as originally proposed by Turcotte et al. (1981). The elastic contributions could
 282 be derived after estimating the elastic properties such as the (time-dependent)
 283 elastic thickness of the lithosphere. But we do not consider this here for simplic-
 284 ity and for the sake of comparability to the study of Steinberger et al. (2010),
 285 who suggested that a purely viscous rather than a viscoelastic model can explain
 286 the long-wavelength gravity and topography on Venus.

287 For comparison to observational data from Venus we use gravity model
 288 SHGJ180U.A01 (available online at http://pds-geosciences.wustl.edu/mgn/mgn-v-rss-5-gravity-l2-v1/mg_5201/gravity/). The topography we use here is ob-
 289 tained from Venus’ shape as given by Wieczorek (2007); these data are avail-
 290

291 able online at [https://markwieczorek.github.io/web/spherical-harmonic-models-](https://markwieczorek.github.io/web/spherical-harmonic-models-topography/spherical-harmonic-shape-models.html)
 292 [topography/spherical-harmonic-shape-models.html](https://markwieczorek.github.io/web/spherical-harmonic-models-topography/spherical-harmonic-shape-models.html). We focus on spectral char-
 293 acteristics here, because our generic numerical model cannot be expected to
 294 reproduce the actual observed venusian gravity and topography patterns in real
 295 space. However, the obtained solutions for Φ_{lm} could in principle be trans-
 296 formed into real space.

297 To quantify how well our model predictions match the present-day observa-
 298 tions, we define the misfit measures δ_G , δ_T , δ_C and δ_R . For example, δ_G is given
 299 as $\delta_G = \left[1/(l_c - 1) \cdot \sum_{i=2}^{l_c} ((P_{gg,i} - P_{gg,i}^*)/P_{gg,i}^*)^2 \right]^{1/2}$, where P_{gg}^* is the gravity
 300 power for present-day Venus. δ_G may thus be interpreted as the average relative
 301 misfit between predicted and observed power spectrum per spherical harmonic
 302 degree. A value of $\delta_G = 0$ implies a perfectly matching model, while a value of
 303 1 means that the misfit has the same amplitude as the respective observational
 304 value. δ_T , δ_C , and δ_R are defined accordingly using either the topography power
 305 spectrum P_{tt} , the degree correlation C_{gt} or the geoid-topography ratio R_{gt} in-
 306 stead of P_{gg} . We chose $l_c = 10$ because we are primarily interested in the misfit
 307 at the longest wavelengths, which are more sensitive of the structure of the
 308 deeper interior. Finally, we note that we will subsequently plot the square root
 309 of P_{gg} multiplied with the factor GM (where G is the gravitational constant
 310 and M is the planetary mass), simply because this measure has the intuitive
 311 unit of meters.

312 **3. Results**

313 *3.1. Stagnant-lid models*

314 *3.1.1. Thermal and magmatic evolution*

315 We first present a reference model (case S2) to demonstrate some general
 316 features of the computed evolutions in the stagnant-lid scenario. Largely, the
 317 thermal evolution is characterised by an initial phase of heating of the mantle
 318 during which the radiogenic heat production dominates over the entire (bulk)
 319 mantle (Figure 1a). A peak in bulk mantle temperature is reached at ~ 3 Ga in
 320 this case, after which the effects of secular cooling and surface heat loss over-
 321 come the heating of the mantle, and mantle temperature starts to drop with an
 322 almost constant rate of $\sim 25 - 30$ K Gyr $^{-1}$. This rather slow rate of cooling is
 323 due to the absence of surface recycling via subduction of lithospheric plates back
 324 into the mantle. Aside from secular cooling that arises from the slow demise of
 325 radiogenic heating, heat is lost by conduction through the lithosphere and by
 326 the extraction of melt. In total, this accounts for an average surface heat flux of
 327 ~ 22 mW m $^{-2}$ at present-day, a factor 4-5 smaller than the average terrestrial
 328 heat flux at present-day.

329 Except during the first billion years of evolution, this value has not been
 330 much different for earlier times, but a general tendency towards a gently in-
 331 creasing surface heat flux (q_s) by a few mW m $^{-2}$ in the second half of the
 332 evolution is apparent (Figure 1b). We attribute this to the slow decrease in
 333 thermal boundary layer thickness with time (Figure 1d), which itself is linked

Case	$\overline{q_S}$	$\overline{q_C}$	M_e^{tot}	δ_G	δ_T	δ_C	δ_R	$\overline{N_{pl}}$	$\overline{d_{cr}}$
S1	25.5	20.8	0.41	0.71	0.47	0.51	0.18	8.8 ± 0.6	109 ± 11
S2	21.9	18.7	0.34	0.52	0.40	0.48	0.25	9.4 ± 0.5	136 ± 15
S2a	23.1	19.2	0.25	1.31	0.74	0.49	0.28	11.5 ± 2.1	131 ± 13
S2b	27.1	19.4	0.31	0.69	0.34	0.49	0.29	8.6 ± 0.6	123 ± 14
S3	18.9	15.9	0.30	1.85	1.52	0.48	0.23	16.0 ± 1.3	168 ± 23
S4	15.1	13.6	0.27	12.2	7.36	0.38	0.51	27.2 ± 2.8	198 ± 26
S5	22.7	16.9	0.40	0.73	0.59	0.57	1.25	7.6 ± 1.5	131 ± 98
S6	21.8	15.5	0.29	2.40	1.45	0.49	0.44	14.6 ± 1.0	139 ± 22
S7	22.2	18.4	0.33	1.02	0.53	0.50	0.36	12.6 ± 0.5	135 ± 17
S8	22.6	17.3	0.31	2.68	0.98	0.73	1.24	13.6 ± 0.6	132 ± 18
E30	42.6	32.6	0.34	1.44	0.41	0.78	0.61	—*	21 ± 7
E50	26.0	15.3	0.30	0.26	0.30	0.33	0.21	—*	62 ± 24
E50a	25.2	15.5	0.22	0.34	0.35	0.43	0.31	—*	58 ± 22
E50b	27.5	14.6	0.30	0.49	0.29	0.22	0.34	—*	44 ± 19
E55	27.5	15.8	0.32	0.55	0.49	0.64	0.24	—*	48 ± 18
E60	29.8	31.2	0.33	0.48	0.88	0.25	0.21	—*	67 ± 50
E70	23.3	16.0	0.30	0.39	0.39	0.44	0.18	—*	114 ± 25

Table 3: Output diagnostics: mean surface heat flux $\overline{q_S}$, mean CMB heat flux $\overline{q_C}$, total cumulative mass of erupted material M_e^{tot} (normalised by the total mantle mass), average deviations from the observed gravity power spectrum δ_G , topography spectrum δ_T , gravity-topography correlation δ_C , and from the observed gravity-topography ratio δ_R , number of detected plumes $\overline{N_{pl}}$ and mean crustal thickness $\overline{d_{cr}}$. If given, \pm -symbols indicate one standard deviation. All values are for $t = 0$ Ga. Heat fluxes are given in mW m^{-2} and crustal thicknesses in km, respectively. For N_{pl} , we provide a mean value and standard deviation from 100 different detection thresholds $\xi_{1,2}$. (* $\overline{N_{pl}}$ is not listed here for episodic cases, because it becomes more time-dependent and sensitive to the detection thresholds.

334 to a slow decrease in melt production and extraction (Figure 1c) and thus in
335 crustal thickness (see section 3.1.3). On the other hand, the heat flux from the
336 core into the mantle decreases by a factor of ~ 3 from 4 Ga until present-day
337 (and by a factor of ~ 2 from 3 Ga, respectively). This is because in the modelled
338 stagnant-lid scenario the mantle does not cool quickly enough, so that internal
339 mantle temperature and CMB temperature slowly adjust (Figure 1d), which
340 effectively reduces the heat flow across this boundary.

341 Some part of the cooling of the mantle is always due to the extraction of
342 hot magma and its emplacement at the surface where it cools quickly (Armann
343 and Tackley, 2012) (assuming that the surface temperature is not substantially
344 higher than for present-day Venus). The magnitude of this contribution depends
345 on the temperature within the upper mantle and thus follows a similar decreasing
346 trend as mantle temperature. The models show that melting and magmatic
347 eruptions are still ongoing at present-day (Figure 1c) and thus contribute to
348 cooling the interior and resurfacing. As a consequence, the entire mantle below
349 the crust is depleted in basalt compared to the initial bulk composition (Figure
350 1e). Melting occurs only in the upper mantle, but mantle flow homogenises
351 composition fairly efficiently, so that no clearly basalt enriched regions seem to

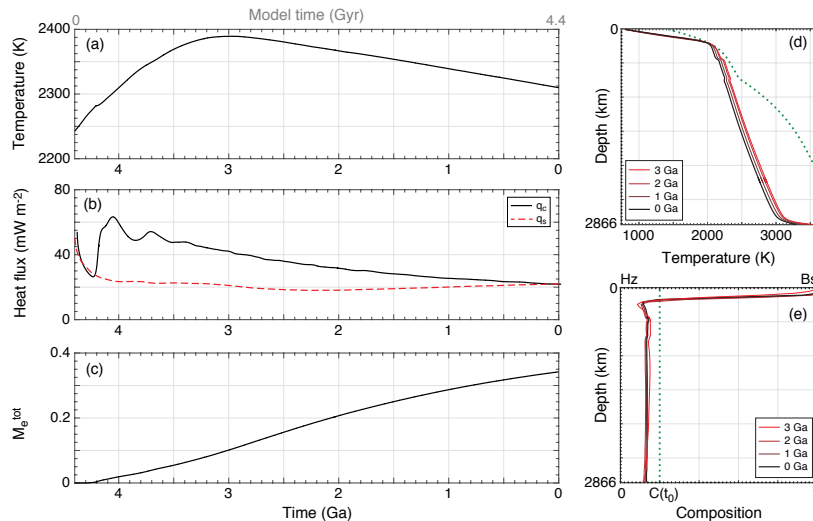


Figure 1: Thermochemical evolution of model S2: (a) Globally averaged internal temperature, (b) average heat flux across surface (q_s) and CMB (q_c), (c) Total mass (cumulative) of erupted material M_e^{tot} normalised by the total mantle mass $M = \int_{V_m} \rho dV$, where V_m is the volume of the modelled spherical shell. Time is typically given in Ga and thus denotes time before present-day. For reference, the time since the start of the model (in Gyr) is indicated on top of panel (a). (d-e) Laterally averaged radial profiles of temperature and composition at different times, respectively. In (d) the dotted line denotes the solidus assuming the initially homogeneous composition shown as a dotted line in (e).

352 exist in this model. Also, the compositional profile does not seem to change
 353 much over the last 2 – 3 Gyr of evolution, which may indicate that crustal pro-
 354 duction and recycling are in approximate equilibrium.

355 The quantitative details of the processes discussed in this section vary to
 356 some degree between the different models of the S-family, like the magnitude of
 357 surface and CMB heat flux, the timing of the thermal maximum and the total
 358 amount of erupted material generated in the course of the evolution. Qualita-
 359 tively, the discussed behaviour seems typical for the stagnant-lid models. Some
 360 related diagnostics are listed in Table 3, but we note that no direct observations
 361 are available on the temperature within the venusian mantle or the heat flux
 362 across the surface.

363 3.1.2. Gravity spectra and gravity-topography relations

364 The model-predicted present-day gravity power spectra and their relation to
 365 topography are presented in Figure 2. A first general observation is that none of
 366 our generic stagnant-lid models resembles the observed gravity power spectrum
 367 closely over the whole range of spherical harmonic degrees $l = 2 - 16$, but some
 368 cases perform significantly better than others (see diagnostics δ_G , δ_T , δ_C and δ_C
 369 in Table 3). Increasing the reference viscosity η_0 has a strong effect on the pre-
 370 dicted gravity spectra by generally increasing the power and by shifting the peak

371 power to somewhat higher spherical harmonic degrees (Figure 2b). Greater vis-
 372 cosity generally enhances convective stresses, which ultimately increases surface
 373 topography in our approach, so that increased gravity power may be somewhat
 374 expected. The shift of the peak power towards higher harmonics (or shorter
 375 wavelength) is less intuitive. Upon cooling with time, however, the mantle flow
 376 pattern typically evolves towards longer wavelength. This happens in all our
 377 stagnant-lid cases, but the process is slower with higher viscosity and cases S3
 378 and S4 may thus still be dominated by too short flow components to explain
 379 Venus’ presently observed topography and gravity spectra. This is also reflected
 380 in the detected number of mantle plumes (see Figure 3 in section 3.1.3). In con-
 381 trast, cases S1 and S2 match the power spectrum significantly better.

382 All four models (S1-S4) feature a high correlation between gravity and topog-
 383 raphy as observed on Venus, but case S1 features somewhat reduced correlation
 384 in the range $l = 5 - 8$ for unknown reasons (Figure 2c). The spectral ratio be-
 385 tween gravity and topography R_{gt} is matched very well by case S2, although this
 386 may exclude the longest wavelength ($l = 2$, Figure 2d). At least for spherical
 387 harmonic degrees $l \leq 10$, case S2 seems to match the characteristics of Venus’
 388 present-day gravity and topography spectra best (see Table 3), although the fit
 389 is clearly not optimal ($\delta_G = 0.52$, $\delta_T = 0.40$, $\delta_C = 0.48$, $\delta_R = 0.25$).

390 Next, we keep η_0 fixed at the value used in case S2, but vary the viscosity
 391 increase with depth by changing the activation volume V_A (Figure 2e). Nei-
 392 ther reducing nor increasing the depth increase of viscosity helps to improve the
 393 match to the observed gravity spectrum though (Figure 2f) or the correlation
 394 to topography and the spectral ratio of the two properties (Figure 2g+h). In
 395 fact, case S2 remains the best matching case. Thus far, we have only varied the
 396 depth gradient, which corresponds to a smooth increase of viscosity with depth.
 397 The viscosity increase may also include discontinuities across interfaces like the
 398 mantle phase transitions. On Earth, for instance, matching the geoid at the sur-
 399 face by dynamic flow models has typically required a significant viscosity jump
 400 across the 660 km phase boundary (e.g. Hager et al., 1985). When introducing
 401 a viscosity jump in our model, the most important consequence is a breakdown
 402 of gravity-topography correlation in the lower spherical harmonics that is the
 403 more pronounced the stronger the viscosity contrast across the 730 km phase
 404 transition is (Figure 2k). This is consistent with the lack of this correlation
 405 on Earth, but does not match the spectral characteristics of Venus as already
 406 suggested by previous studies (e.g. Steinberger et al., 2010; Huang et al., 2013).

407 Finally, changing the parameters H_P and ΔH (see section 2) causes a slightly
 408 different thermal evolution. In both cases this leads to a somewhat reduced man-
 409 tle temperature and correspondingly higher average mantle viscosity, but the
 410 effects seem rather small compared to those explained above (Figure 2m). The
 411 density anomalies defined by cases S2, S2a and S2b still differ, however, which
 412 may explain the difference in the predicted spectra (Figure 2n-p).

413 3.1.3. Number of mantle plumes

414 We now investigate the number of mantle plumes in the stagnant-lid evo-
 415 lutions (S1-S8), which has recently been used as a constraint on the venusian

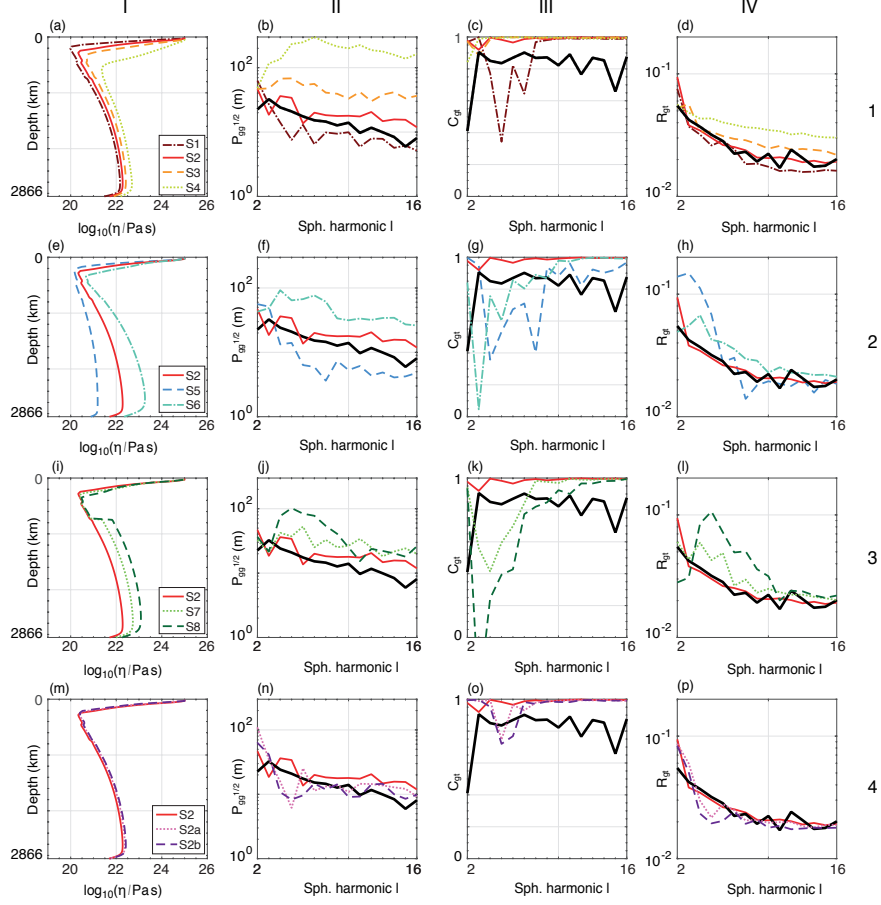


Figure 2: Gravity field spectral analysis for the stagnant-lid cases S1-S8 in comparison to observations for present-day Venus (thick black lines). Each row denotes a different family of cases in which a different parameter is varied: (Row 1) reference viscosity η_0 , (Row 2) activation volume V_{A0} , (Row 3) viscosity jump across the phase transition to perovskite. In (Row 4), a lower internal heating rate (parameter H_P , case S2a) or a stronger partitioning of radiogenic elements into the basaltic material (parameter ΔH , case S2b) has been employed. Each column I-IV displays a different measure: (I) present-day radial viscosity profiles; (II) the square-root of the present-day gravity power spectra P_{gg} as defined in the text, (III) the degree correlation between gravity and topography C_{gt} and (IV) the spectral ratio R_{gt} of gravity and topography.

416 volatile history (Smrekar and Sotin, 2012) and mantle viscosity structure (Huang
417 et al., 2013). Mantle plumes may be linked to anomalies in Venus’ surface ther-
418 mal emissivity and only nine of them have been detected by the VIRTIS exper-
419 iment on Venus Express (Smrekar et al., 2010). To accomplish this, we follow
420 the methodology of Huang et al. (2013) and track hot mantle plumes based on
421 their temperature and radial velocity characteristics. A hot plume is detected,
422 when the local temperature T_{loc} at the depth of interest is significantly larger
423 than the average (T_{avg}) at this depth: $T_{loc} > T_{avg} + \xi_1(T_{max} - T_{avg})$, where
424 T_{max} denotes the maximum temperature at this depth. The same criterion is
425 used for radial velocity instead of temperature. For the plume regions detected
426 by this method, we compute the plume flux and subsequently ignore all small
427 plumes for which this flux is smaller than a fraction ξ_2 of the maximum flux.
428 Following Huang et al. (2013), we chose $\xi_1 = 0.2$ and $\xi_2 = 0.05$, but we repeat
429 the detection 100-times and let $\xi_{1,2}$ vary by up to $\pm 50\%$ around these central
430 values in order to evaluate the sensitivity of results with respect to our choice
431 of $\xi_{1,2}$. If not stated otherwise, the number of plumes is analysed at a depth
432 of ~ 970 km. We chose this rather deep detection layer because we are mostly
433 interested in the major mantle plumes; towards shallower depth, the thermal
434 structures are typically smaller-scale because of the lower viscosity and the ac-
435 tion of magmatic processes, and it becomes more difficult to detect the relevant
436 anomalies with our simple approach (Figure 3a-c).

437 We find that the uncertainty caused by the assumed $\xi_{1,2}$ is rather small in
438 the stagnant-lid cases (except perhaps for the high-viscosity case S4): the com-
439 puted standard deviation is typically 10% or less of the mean value (Table 3 and
440 Figure 3d). Within the last billion years, the number of detected plumes does
441 not seem to vary much in most cases, but during earlier phases of the evolution
442 their number tends to be higher (by a factor of 1.5-2.5, Figure 3e). The initial
443 plumes may then slowly merge to more pronounced groups in response to the
444 long-term cooling of the mantle, which effectively decreases convective vigour.
445 This process of plume merging seems to occur somewhat faster the less viscous
446 the mantle is, which may explain why the number of computed mantle plumes
447 for the present-day increases with the reference viscosity η_0 (cases S1-S4, Figure
448 3d). In fact, in the highest viscosity case (S4) the process of plume merging is
449 probably far from being completed at $t = 0$ Ga.

450 A further, but less pronounced trend is that the number of detected plumes
451 tends to increase with stronger viscosity stratification at depth. The trend seems
452 to hold for both purely gradual and mixed gradual-discontinuous increases (com-
453 pare cases S5-S2-S6 and S2-S7-S8 in Figure 3d, respectively). This would be
454 in line with the argument in the previous paragraph since a stronger viscosity
455 gradient would cause a more viscous lower mantle which probably controls the
456 mobility of plume conduits that originate from the CMB.

457 The cases for which the spectral characteristics of gravity and topography
458 were matched best (cases S1 and S2) also seem to comport with the VIRTIS
459 constraint of approximately nine detected high thermal emissivity regions. This
460 is not surprising since Venus’ long-wavelength gravity spectrum is tied to the
461 structure of mantle flow (Steinberger et al., 2010) of which the number and

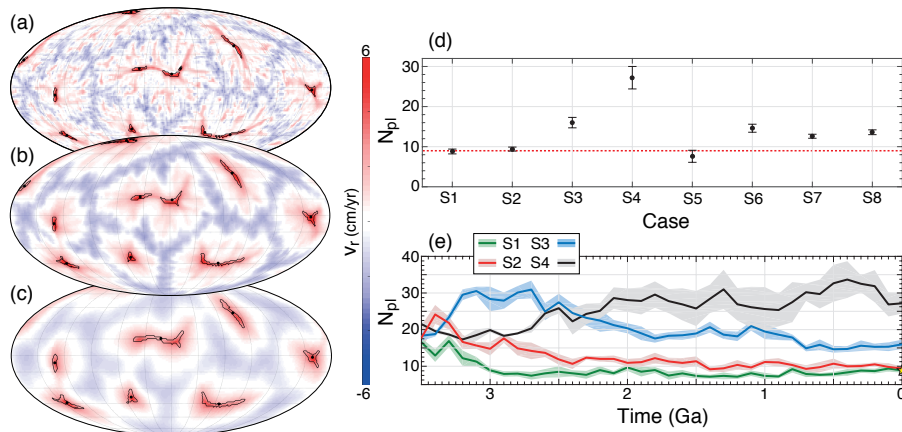


Figure 3: Mollweide projections of radial velocity v_r (colour-coding) at depths of (a) ~ 590 km, (b) ~ 940 km, (c) ~ 1850 km (case S2 at present-day); $v_r > 0$ denotes upward motion. Black contours indicate detected plume regions whose centroids are depicted by black dots. Here, the detection parameters $\xi_1 = 0.2$ and $\xi_2 = 0.05$ are used (following Huang et al., 2013). (d) Number of detected plumes N_{pl} at present-day for cases S1-S8. The dots indicate the mean values of 100 estimations with different ξ_1, ξ_2 , which have been varied randomly by up to $\pm 50\%$ from the values used in (a)-(c). The error bars depict the corresponding standard deviations. In (d), the dotted horizontal line is an estimate for present-day Venus using thermal emissivity constraints (Smrekar et al., 2010). (e) Time variation of N_{pl} since 3.5 Ga for cases S1-S4 in 100 Myr increments. Bold lines indicate the mean number of plumes \bar{N}_{pl} , the shaded margins the standard deviation at the respective time step.

462 positioning of plumes is a representation. In contrast to the gravity spectrum,
 463 the number of plumes is an indirect observation since the proposed link between
 464 thermal emissivity anomalies and deep mantle plumes (see Smrekar et al., 2010)
 465 cannot be rigorously tested with existing available data. Accordingly, the num-
 466 ber of plumes may thus not be as constraining for Venus evolution models as
 467 the gravity observation. Yet, our finding that reduced mantle viscosities are
 468 favourable for matching Venus' rather small number of plumes is generally con-
 469 sistent with the results of Smrekar and Sotin (2012), although these authors
 470 suggest the need of even lower mantle viscosity ($\leq 10^{20}$ Pa s) if strong inter-
 471 nal heating is present. All our models are dominantly internally heated, but
 472 they also feature significant (gradual) viscosity variation below the lithosphere,
 473 which is known to affect the wavelength of convection. In this combination,
 474 which was not investigated by Smrekar and Sotin (2012), it seems possible to
 475 predict Venus' number of mantle plumes without the need of such very low
 476 mantle viscosities.

477 3.2. Episodic evolutions

478 3.2.1. Thermal and magmatic evolution

479 In the models described above, the lithosphere remained in a stagnant-lid
 480 state throughout the entire evolution, such that large-scale recycling of the

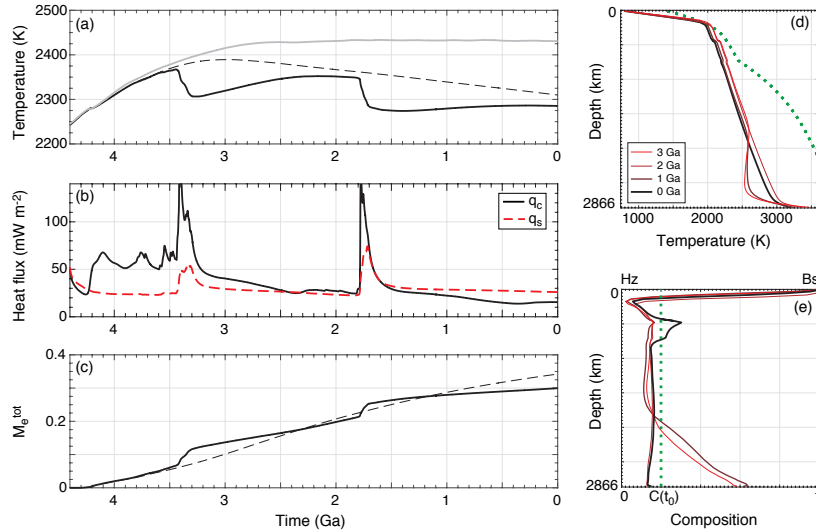


Figure 4: As in Figure 1, but for the episodic model E50. In (a) and (c), the results for the stagnant-lid evolution S2 are given for comparison as a dashed line. In (a), we also show the result for case E50 recomputed without the basalt-eclogite phase transition in grey.

481 surface by tectonic processes was inhibited. In this section, we present the
 482 other class of evolution models with phases of rapid surface mobilisation, which
 483 lead to tectonic recycling of parts or the entire surface. Here, we focus on
 484 episodic evolutions that have clearly distinguishable overturn events, separated
 485 by elongated phases of stagnant-lid convection since this allows us to investigate
 486 the overturn events and their aftermath in detail. For this purpose, we tune the
 487 yield stress of the lithosphere (σ_0) to reach such a scenario, but note that the
 488 number, duration and frequency of such overturn events in Venus' history are
 489 unknown.

490 Case E50 features two major overturns the first of which initiates at ~ 3.4 Ga,
 491 the second one at ~ 1.8 Ga (Figure 4). Upon recycling of cold surface material
 492 into the deeper interior, the mean temperature of the mantle drops (Figure 4a)
 493 and heat transport across the boundary layers becomes more efficient (Figure
 494 4b). During the overturn, the total heat flux across the surface may be $2 - 3\times$
 495 higher than before the overturn. The heat flux increase is even stronger for the
 496 bottom heat flux once cold recycled material comes to rest on the CMB, which
 497 temporarily increases the temperature drop across this boundary (Figure 4d+e).
 498 In addition to the temporary accumulation of basaltic components at great
 499 mantle depth after the overturn event, this material can also become relatively
 500 enriched in the mantle transition zone as a consequence of the basalt barrier
 501 mechanism stating that basalt is not buoyant at this depth (Papuc and Davies,
 502 2012).

503 *3.2.2. Overturn evolution*

504 As in the stagnant-lid evolutions described above, melting and its extraction
505 and thus magmatic surface recycling is ongoing throughout the entire evolu-
506 tion, but it peaks during the overturns and then happens at a clearly reduced
507 rate after the overturn, also compared to the rate in the stagnant-lid evolution
508 (Figure 4c). At present-day, however, the difference in total cumulated erupted
509 material between cases S2 and E50 seems rather small ($\sim 10 - 15\%$, Table 3).

510 Generally, the overturn events in our model are typically triggered by the
511 growth of crust. Upon ongoing melt extraction from the interior, the basaltic
512 crust on the surface grows thicker. Once crustal thickness exceeds the eclogite
513 phase transition at ~ 65 km depth, the crust becomes more and more negatively
514 buoyant and the resulting stresses in the lithosphere overcome the yield strength
515 at some point. The importance of this process is additionally highlighted by the
516 fact that recomputing the same model without the basalt-eclogite transition did
517 not feature any overturn event (Figure 4a).

518 The overturn events may thus initiate locally according to the crustal and
519 stress distribution. Once initiated the stress pattern induced to the lithosphere
520 changes and lithospheric failure propagates rapidly across the surface (Figure
521 5). This process typically affects the surface globally, but we have not explicitly
522 investigated here, whether parts of the surface may resist recycling during the
523 overturn.

524 During the overturn, the surface is mobilised and may on average move as
525 fast as ~ 20 cm/yr. The duration of surface mobilisation is $\sim 150 - 200$ Myr
526 (Figure 5e). In fact, this duration is very similar to what has been observed
527 in corresponding 2D evolutions of Armann and Tackley (2012), which is some-
528 what surprising as one may expect a more complex propagation of resurfacing in
529 3D and thus a longer time required for global resurfacing. This may point to a
530 rather symmetric style of overturn propagation that can be reasonably captured
531 also by 2D models. The value of the yield stress (σ_0) does not seem to affect
532 this behaviour very much; the main consequence of changing σ_0 is a change in
533 timing and perhaps the frequency of the overturns: with higher yield stress, the
534 lithosphere can sustain the stress induced by mantle flow and crustal growth for
535 a longer time.

536 It is interesting to note that the 2D models of Armann and Tackley (2012)
537 predict 5 – 8 overturns for a typical evolution of Venus. In contrast, our 3D
538 models predict only 1 – 3 overturns. Clearly, this depends on the details of the
539 model setup and the resulting stresses in relation to the yield stress, although
540 lowering its value in our models does not seem to lead to a significantly increased
541 number of clearly distinguishable overturns. Instead, the system may fall into
542 a state of (somewhat Earth-like) continuous recycling at some point (case E30
543 in Figure 5e, which has a 40% reduced yield stress compared to the reference
544 model). This may point towards a different time-dependence in 2D and 3D
545 models as was already suggested by Huang et al. (2013), although their models
546 did not feature lithospheric overturn.

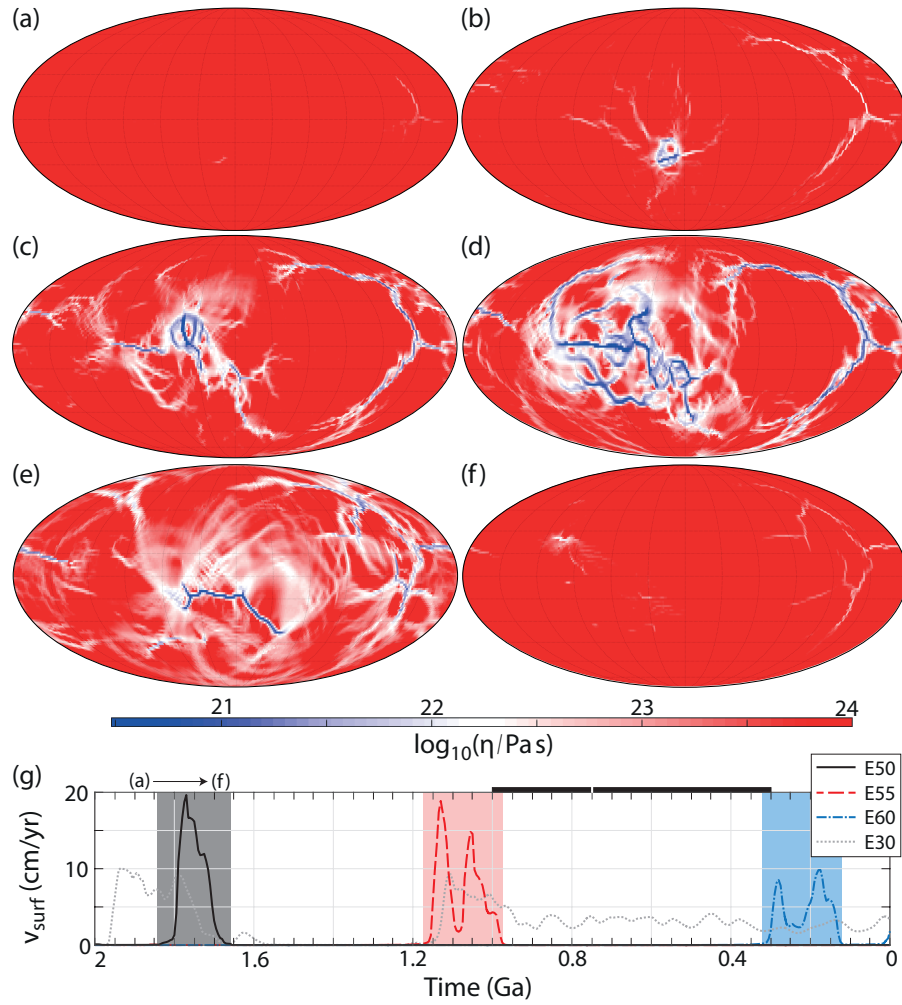


Figure 5: Overturn evolution (case E50). Mollweide projections of surface viscosity at different times: (a) 1.90 Ga, (b) 1.82 Ga, (c) 1.79 Ga, (d) 1.78 Ga, (e) 1.71 Ga, (f) 1.68 Ga. (g) Time evolution of rms-surface velocity (smoothed) since 2 Ga for four cases with different surface yield stress σ_0 as indicated. The black solid curve corresponds to the evolution shown in (a)-(f). The shaded regions indicate the time period during which surface velocities are significantly increased due to the overturn. Note that Case E70 is not shown here, because it does not show significant surface mobilisation after 2 Ga, its last overturn fades around 2.4 Ga. For the other cases, the last overturn falls in the plotted time span. Venus' mean surface age (white mark) and its uncertainty range (black horizontal bar) as inferred from cratering statistics (McKinnon et al., 1997) are indicated on top of panel (g).

547 *3.2.3. The aftermath of an overturn event*

548 As described in the previous section, the overturns can be seen as extreme
549 events that globally perturb the background dynamics of the planet’s interior.
550 Thus, they introduce additional time scales into the thermal evolution, which
551 are related to the frequency of overturn events and the time scale over which
552 they may affect the planetary interior. Especially this latter time scale is of
553 great interest for the interpretation of present-day planetary observations, such
554 as gravity. As indicated above, overturns mobilise the surface globally and the
555 duration of these mobilisation periods is estimated to be 150 – 200 Myr based
556 on our modelling. However, the recycled surface material may affect the state
557 of the interior over a longer time period and this could be detectable in surface
558 observables.

559 An analysis of the spectral characteristics of gravity and topography in some
560 of our episodic cases is given in Figure 6. Again, several major observations can
561 be made. First, with a too low yield stress that leads to an almost continuously
562 overturning evolution (case E30), the cold recycled surface material leads to a
563 stronger viscosity increase with depth (Figure 6a). As a consequence, the power
564 spectrum of gravity decreases more strongly with increasing harmonic degree l
565 and results in a strongly ($l = 2$)-dominated planet with comparably large misfit
566 to the observed spectra (Table 3 and Figure 6b). In liaison, the correlation be-
567 tween gravity and topography in the low degree range breaks down as already
568 observed in stagnant-lid models with strong viscosity increase with depth (Fig-
569 ure 6c). This clearly points to a more Earth-like rather than a Venus-like model.
570 Similar effects, though somewhat less pronounced, can be observed for case E60
571 in which the latest overturn faded only very recently (Figure 5g) and regions
572 of anomalously high viscosity in the lower mantle caused by cold recycled ma-
573 terial still persist. On the other hand, some of the episodic cases in which the
574 latest overturn event happens sufficiently long ago, generate an equally good or
575 even better match to Venus’ observed gravity spectrum than our most successful
576 stagnant-lid model (S2). For example, case E50 predicts the smallest misfits in
577 the gravity $\delta_{gg} = 0.26$) and topography spectra ($\delta_{tt} = 0.30$) across our suite
578 of cases. Perhaps the most remarkable difference is that the successful episodic
579 cases also produce the observed peak in the gravity spectrum at spherical har-
580 monic degree $l = 3$ and the relatively lower power at $l = 2$ (Figure 6b), which
581 typically did not evolve in the stagnant-lid models (Figure 2). We note though
582 that this ($l = 3$)-dominance is only featured during a small part of the evolution
583 since the last overturn event (Figure 6e), so the relevance of this observation is
584 difficult to infer.

585 Clearly, the overturn event strongly perturbs the gravity power spectrum at
586 all wavelengths. At the longest wavelengths ($l = 2 - 3$), the peak power during
587 the overturn may be 1-2 orders of magnitude above the pre- and post-overturn
588 level (Figure 6e), although the quantitative increase most likely depends on the
589 details of our model. However, this peak is rather short and mostly coincides
590 with the period of surface mobilisation. Some increased power in $l = 2 - 3$
591 may still be visible after the surface motion has terminated, but is limited to

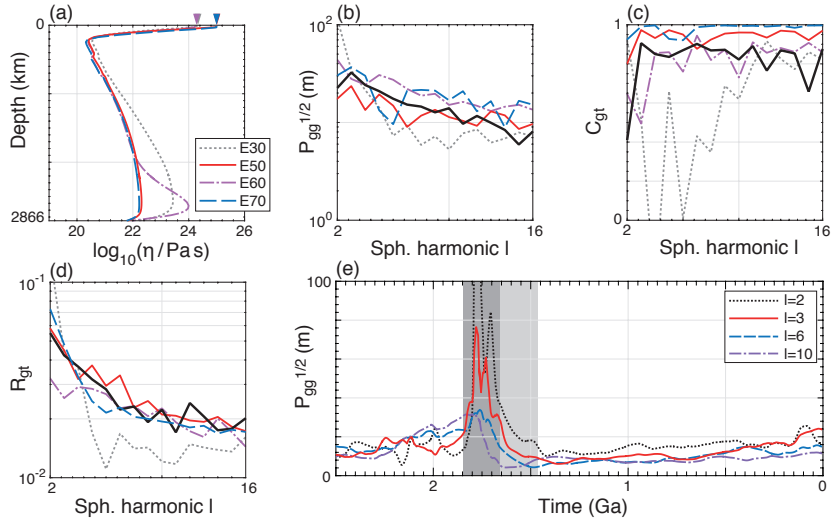


Figure 6: Spectral analysis for episodic cases: (a)-(d) correspond to panels (a)-(d) in Figure 2, but depict cases E30, E50, and E70 with different values of surface yield stress σ_0 . (e) Time evolution of the power in spherical harmonic degrees $l = [2, 3, 6, 10]$ since 2.5 Ga. The dark-shaded region indicates when the surface is substantially mobilised (compare to Figure 5), the light-shaded region indicates for how much longer the gravity power for $l = 2 - 3$ still differs from the pre-overturn level.

592 $\sim 100 - 200$ Myr. This is probably the case, because the cold surface material
 593 sinks rather rapidly through the mantle given our preferred viscosity profile
 594 without strong discontinuities. Such material will come to rest on top of the
 595 CMB (Figure 4e), but the surface gravity is rather insensitive to density anomalies
 596 in this lowermost depth range and certainly only at the longest wavelengths
 597 (e.g. Hager et al., 1985).

598 Such deeply recycled material on top of the CMB may also affect the CMB
 599 heat flux and the structure of the bottom boundary layer which in turn controls
 600 the initialisation of mantle plumes (Figure 7). Some time after the onset of the
 601 overturn, the recycled basaltic material will cover the major part of the CMB
 602 thereby annihilating the pre-overturn plume pattern. In the following, plumes
 603 have to initialise again, initially on small-scale. The number of plumes detected
 604 by our simple approach is very high then (Figure 7d), but their actual number
 605 is quite dependent on the detection parameters $\xi_{1,2}$. The key observation, how-
 606 ever, is that their number recovers to approximately pre-overturn level once the
 607 recycled material has entrained into shallower mantle layers again (Figure 7e).
 608 In our models, this process requires a rather long time of 1 Gyr or even more,
 609 but again, this will depend on the detailed density structure of the models and
 610 also the temperature at the CMB. Further systematic exploration of such pa-
 611 rameters is necessary to further refine our general observation. If this holds true
 612 though and the number of mantle plumes is in addition indeed related to sur-
 613 face thermal emissivity anomalies, such a long overturn relaxation time could

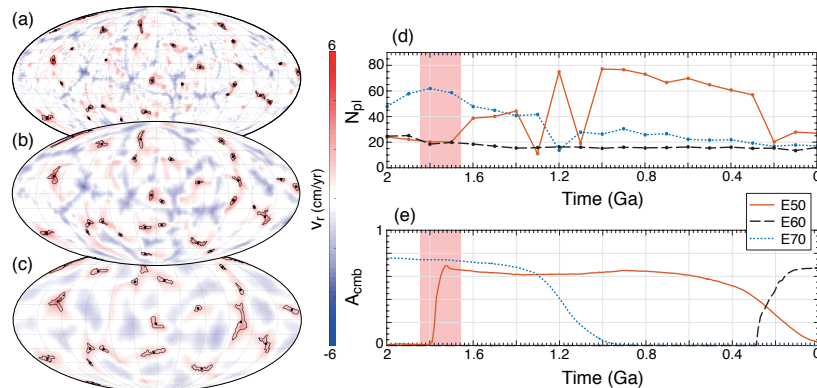


Figure 7: (a)-(c) As in Figure 3a-c, but for episodic case E50. (d) Time evolution of the mean number of detected plumes (\overline{N}_{pl}) since 2 Ga in episodic cases E50, E60 and E70. (e) Fraction of the CMB area (A_{cmb}) covered by basaltic material. The shaded region indicates the period of major surface mobilisation for case E50.

614 favour a rather long-ago cessation time of Venus' latest overturn event. We
 615 note that it can also take some time after the overturn onset until the number
 616 of plumes increases substantially. Possibly, not all overturn events disturb the
 617 plume pattern equally strong (e.g., see evolution E60 since ~ 0.4 Ga in Figure
 618 7d). This may depend on where the resurfacing event initiates and then how it
 619 propagates across the surface in relation to the plume pattern. Inferring these
 620 details is beyond the scope of the present study, but without them it is probably
 621 difficult to infer overturn cessation time from the plume pattern, respectively
 622 from the number of plumes.

623 3.3. A stagnant or an episodic lid scenario for Venus?

624 3.3.1. Crustal thickness evolution

625 So far, we have presented the differences between the stagnant-lid and episodic
 626 scenario, but it would be desirable to constrain which of these may be more ap-
 627 plicable for Venus' evolution. One diagnostic to discuss is crustal thickness,
 628 which is essentially given by the local thickness of the surface layer of basaltic
 629 crust which has been extracted from the interior upon melting (see e.g. Keller
 630 and Tackley, 2009). Here, we are mostly interested in its spatial mean value and
 631 its standard deviation (see Table 3 for quantitative results).

632 Due to our initial condition, crustal thickness is initially zero in all our mod-
 633 els until the onset of melting processes, that is after ~ 100 Myr. From then
 634 on mean crustal thickness increases for 1 – 2 Gyr for the stagnant-lid models
 635 until a maximum is reached (Figure 8a), afterwards mean crustal thickness ap-
 636 pears rather constant indicating a balance between production of new crust due
 637 to melt extraction and destruction of crust by convective erosion and drip-off
 638 of the dense eclogitic base of the crust (see also Armann and Tackley, 2012).
 639 The slight decrease of crustal thickness towards modern times as observed in

640 some cases is probably an expression of secular cooling due to which magmatism
641 slowly fades (Figure 1).

642 In none of the stagnant-lid cases a present-day mean crustal thickness of
643 less than 100 km can be observed, which is significantly above previous inde-
644 pendent estimates (e.g. Anderson and Smrekar, 2006; James et al., 2013; Wei
645 et al., 2014). This may mean that too much melting is generated in our model
646 (or at least erupted onto the surface). We tried to reduce the amount of melting
647 by allowing for enrichment of radiogenic heat sources in the basaltic component
648 (case S2b), so that they should concentrate in the crust in the course of the
649 evolution. Yet, this seems to only marginally reduce crustal thickness, similar
650 to the findings of Armann and Tackley (2012) in 2D models. Even reducing the
651 (present-day) bulk internal heating rate by 20% does not reduce present-day
652 mean crustal thickness greatly, but mostly effect the timing of crustal growth
653 (case S2a in Figure 8a).

654 In the episodic models much reduced crustal thickness can be achieved, again
655 mostly depending on the timing of the last overturn event (Figure 8b). In the
656 stagnant-lid phases of these evolutions, crustal thickness grows according to the
657 rate of melt extraction. Too thick eclogitic crust, however, triggers an over-
658 turn to reset crustal thickness. It still remains difficult to generate really small
659 average crustal thicknesses, probably because overturn events also feature sub-
660 stantial magmatism and new crust will already be emplaced somewhere, while
661 recycling is on-going elsewhere. Consistent with Armann and Tackley (2012),
662 we note that the episodic cases can still feature some eclogitic crustal base to
663 some extent, probably because the crust is embedded in a thicker lithosphere
664 which prevents efficient basal recycling of the crust.

665 Nevertheless, several of our episodic evolutions generate present-day mean
666 crustal thicknesses that reasonably overlap with other estimates. As in the
667 stagnant-lid models, we tested also the effect of reduced bulk internal heating
668 and abundance of radiogenic elements in the crust (cases E50a and E50b). Both
669 tend to reduce the effective growth rate of crust in the stagnant-lid phases of
670 the evolutions, however, the time that has passed since the last overturn seems
671 to be the most important controlling parameter.

672 *3.3.2. Mean surface age*

673 Another important constraint on Venus' evolution comes from its impact
674 crater population, which cannot be distinguished from a random distribution
675 (Herrick, 1994). This and the relatively small number of craters (less than 1000)
676 has lead to the view that Venus' surface has a spatially rather uniform mean age
677 of $0.75_{-0.45}^{+0.25}$ Gyr (McKinnon et al., 1997), although the degree of uniformity and
678 its spatial scales is an issue of on-going research (e.g. Kreslavsky et al., 2015,
679 also see discussion in section 4.2). This relatively young age implies substantial
680 resurfacing during Venus' evolution. While an evolution with catastrophic over-
681 turns seems more feasible to achieve the observed characteristics (e.g. Romeo
682 and Turcotte, 2010), it may also be possible to achieve these via equilibrium
683 resurfacing, for example via volcanic activity (e.g. Bjonnes et al., 2012).

684 Our numerical models allow us to compile global age distributions at any

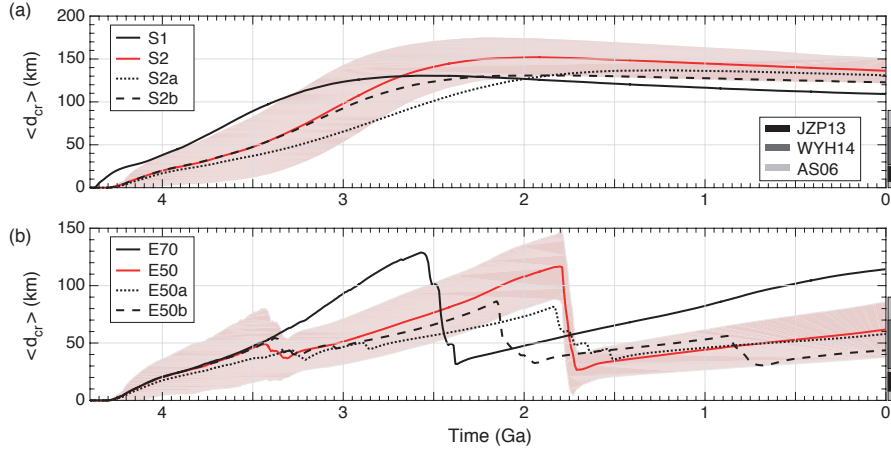


Figure 8: Evolution of modelled mean crustal thickness $\langle d_{cr} \rangle$ for (a) stagnant-lid cases and (b) episodic-lid cases as indicated in the legend. Lines depict the computed mean ages, the shaded areas indicate the standard deviation for cases S2 and E50, respectively. The grey bars on the right y-axis denote independent estimates from the literature (JZP13: James et al., 2013), (WYH2014: Wei et al., 2014), (AS06: Anderson and Smrekar, 2006).

685 given time of the evolution and thus provide important insight into the origin of
686 Venus' present surface age spectrum. We extract surface age from our models by
687 tracking the time a tracer particle has spent in the topmost cell of the numerical
688 grid and averaging the age over all tracer particles within each surface grid cell.
689 This method captures recycling via both magmatism and lithospheric overturn
690 the latter of which has been ignored in previous efforts to analyse Venus' surface
691 age with convection models (Noack et al., 2012). But our simple approach has
692 also limitations and typically leads to somewhat noisy surface ages that can
693 vary strongly over short length scales. The mean age \bar{A} , however, seems to be
694 a rather robust estimate independent of these small-scale fluctuations.

695 As a typical stagnant-lid evolution, case S2 features a mean surface age of
696 $\bar{A} \sim 0.25 \pm 0.18$ Gyr. This mean value does not seem to vary strongly (less than
697 a factor of 2) within 4 Gyr of model evolution (Figure 9). Reducing the amount
698 of melting and thus the efficiency of magmatic surface recycling by reducing the
699 bulk internal heating rate (case S2a) and by increasing the abundance of heat-
700 producing elements in the basaltic crust (case S2b) helps to increase the mean
701 age slightly, but not to more than 0.30 – 0.35 Gyr. In contrast, the episodic
702 model E50 features substantially larger mean age ($\bar{A} \sim 0.60 \pm 0.40$ Gyr) for the
703 present venusian surface to which it has evolved from the latest overturn that
704 happened at ~ 1.8 Ga. During the overturn, surface age is reset to almost zero
705 as expected.

706 We note that the predicted present-day mean age is significantly less than
707 the time passed since the latest overturn, which indicates the strong role of
708 magmatic resurfacing in our models. This may also explain why the surface age

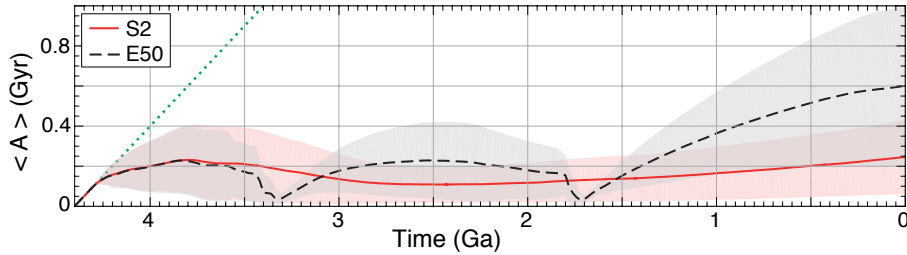


Figure 9: Time evolution of mean surface age $\langle A \rangle$ for (a) case S2, (b) case E50. The shaded areas indicate the respective standard deviation. The vertical bar on the right indicates the proposed range of Venus’ present mean surface age (e.g. McKinnon et al., 1997). The dotted line indicates the maximum possible age (i.e., the complete absence of resurfacing).

709 distribution appears far from uniform as indicated by the rather strong lateral
 710 variation (Figure 9) as ongoing volcanism will degrade the age distribution af-
 711 ter the overturn. As indicated by the rather larger standard deviations as given
 712 above ($\sim 75\%$ and $\sim 66\%$ with respect to the respective mean age), none of our
 713 models is currently able to meet the uniformity constraint of Venus’ present-day
 714 surface in a strict sense. More research is required to understand which con-
 715 ditions are feasible to achieve age distribution with both reasonable mean age
 716 and small lateral variation in our model (see section 4.3), but we also deem it
 717 necessary to further evaluate the degree of age uniformity on current Venus and
 718 over which length scales it may apply.

719 4. Discussion

720 4.1. Venus’ mantle viscosity structure and its implications

721 Based on the ability of our models to match present-day surface observa-
 722 tions, we deem case E50 as most representative for Venus’ evolution at least in
 723 its later stages following the last overturn event. This case predicts a minimum
 724 viscosity of $\sim 2 \times 10^{20}$ Pa s in Venus’ shallow sublithospheric mantle at ~ 200 km
 725 depth. This depth of minimum viscosity seems consistent with the lithospheric
 726 thickness estimate at ~ 200 km of Benesova and Cizkova (2012), who also used
 727 a 3D spherical convection model to infer mantle viscosity from gravity observa-
 728 tions, but did not consider thermochemical effects, melting and magmatism. On
 729 the other hand, Orth and Solomatov (2011) suggested a lithospheric thickness
 730 of up to 600 km based on the assumption that Venus long-wavelength topogra-
 731 phy is mostly explained by isostatically compensated variations in stagnant-lid
 732 thickness. From the shallow minimum, viscosity then increases gradually with
 733 depth by a factor of ~ 100 to a depth of ~ 2600 km (or ~ 250 km above the
 734 CMB) in our model.

735 This preferred viscosity profile is almost identical to the one inferred by
 736 Steinberger et al. (2010), based on mineral physics constraints (Steinberger and
 737 Calderwood, 2006). In contrast to their work, which tended to overpredict

738 Venus' gravity power spectrum at longest wavelength, $l = 2 - 4$, our thermo-
739 chemical forward modelling approach is also capable of reasonably matching the
740 power spectrum and its relation to topography at these spatial scales (Figure
741 6). This includes the absence of a ($l = 2$)–dominance, at least intermittently,
742 which is one of the striking differences between the gravity spectra of Venus and
743 Earth (and in fact also of Mars, Mercury and the Moon).

744 Steinberger et al. (2010) based their findings on geoid and topography ker-
745 nels, which do not consider lateral variations in viscosity, which are present in
746 our approach. However, lateral variations have probably a minor effect on the
747 surface gravity and topography at the longest wavelength compared to radial
748 variations (Richards and Hager, 1989). In addition, the magnitude of lateral
749 viscosity variations in the absence of subducting slabs or large-scale chemical
750 heterogeneity is probably small anyway within Venus' deep interior compared
751 to Earth's. Steinberger et al. (2010) assumed that mantle density heterogene-
752 ity has the same spectral characteristic on present Earth and Venus instead of
753 computing the evolution of density heterogeneities forward in time as we have
754 done here. This may explain parts of the difference in predicted gravity power
755 at long-wavelength between Steinberger et al. (2010) and our model. By as-
756 suming the same spectral and depth dependence of density anomalies for both
757 planets, Steinberger et al. (2010) implicitly considered the decrease of thermal
758 expansivity with depth. Reduced thermal expansivity in the deep mantle could
759 reduce the magnitude of density anomalies there, which would relatively reduce
760 the power in the lowest degrees of the gravity spectrum (only the longest wave-
761 lengths are sensitive to the deep mantle). On the other hand, lower expansivity
762 would reduce convective vigour in the lower mantle, which could give rise to
763 a less time-dependent and longer-wavelength flow pattern that reinforces the
764 power in the lower degrees. Which of these effects may dominate is undeter-
765 mined at this stage and requires further modelling in future. Finally, we note
766 that all models of Steinberger et al. (2010) assumed a stagnant-lid scenario in
767 which our models also tend to overpredict the spectrum at least at $l = 2$ (Fig-
768 ure 2), perhaps because this essentially implies infinite material strength which
769 could alter the stress patterns in the lithosphere.

770 On the other hand, several studies have recently demonstrated that dynamic
771 forward modelling of venusian mantle convection in the stagnant-lid regime has
772 the ability to predict the long-wavelength power spectrum closely (e.g. Benesova
773 and Cizkova, 2012; Huang et al., 2013). While these studies also consider self-
774 consistent thermal evolution of the venusian mantle in 3D, even with lateral
775 viscosity variations (Huang et al., 2013), they did not consider an evolutionary
776 framework as we have done here, including secular cooling, compositional varia-
777 tion, melting and overturn events. Interestingly, Huang et al. (2013) inferred an
778 almost flat viscosity profile below the lithosphere with a total viscosity increase
779 of a factor of ~ 5 towards the CMB, which is lower or on the very low end of
780 what has been found in our and other previous studies (e.g. Pauer et al., 2006;
781 Benesova and Cizkova, 2012). Huang et al. (2013) highlight the importance of
782 phase transitions and their properties in this matter, which have been neglected
783 by various studies (e.g. Benesova and Cizkova, 2012). However, they required a

784 large Clapeyron slope for the transition to perovskite ($\gamma_{ol730} = -3.5 \text{ MPa K}^{-1}$).
785 This is larger than the value we have used here ($\gamma_{ol730} = -2.0 \text{ MPa K}^{-1}$). This
786 value also seems rather large compared to inferences from recent experiments
787 (e.g. Kojitani et al., 2016), unless the mantle at the transition pressure is suffi-
788 ciently hydrous, which may increase the absolute value of γ to levels comparable
789 to their choice (Ghosh et al., 2013). On the other hand, such a hydrous mantle
790 may not be expected for Venus (e.g. Grinspoon, 1993).

791 If such details of the phase transitions explain why Huang et al. (2013)
792 were able to use a much smaller viscosity increase with depth to match Venus'
793 observed gravity spectrum, then more future effort should indeed be spent to
794 improve the treatment of mineral physics in mantle convection models in order
795 to capture their impact on mantle dynamics sufficiently well. Already, Armann
796 and Tackley (2012) reported that mineral phase transitions increased the time-
797 dependence in their 2D models, although this has not been observed in the
798 (simpler) 3D models of Huang et al. (2013). We have not varied phase transi-
799 tion parameters here, so cannot assess this question directly. Still, our models
800 support the importance of phase transitions in the sense that the basalt-eclogite
801 transitions seems to be the dominant trigger for overturn events (Figure 4), al-
802 though this transition is only relevant at shallow rather than mantle transition
803 zone depth.

804 In line with some previous work on Venus' mantle viscosity structure as
805 cited in the previous paragraphs, our models confirm that no significant vis-
806 cosity discontinuity across the transition zone should exist, because it seems at
807 odds with the high correlation between geoid and topography as inferred for
808 Venus. This points to important differences in the internal mantle structure
809 of Earth and Venus, since for the Earth a viscosity jump across the transi-
810 tion zone is typically necessary to fit the surface geoid observation (e.g. Hager
811 et al., 1985). Possibly, the structural difference between the two bodies can be
812 explained by a hydrous terrestrial upper mantle and transition zone, perhaps
813 due to subduction-triggered water cycling, and a relatively dry upper mantle
814 in Venus due to the absence of such a process. Venus' interior may have been
815 dried out additionally by an early large impact (Davies, 2008). In fact, the
816 on-going magmatism in the upper mantle suggested by our models (Figures 1c
817 and 4c) would lead to outgassing of volatiles and water and a rather dry up-
818 per mantle (e.g. Grinspoon, 1993; Smrekar and Sotin, 2012), although probably
819 not entirely dry (Elkins-Tanton et al., 2007). If the lower mantle is compar-
820 ably dry as Earth's (e.g. Murakami et al., 2002), this could explain a relatively
821 smooth viscosity increase with depth in the venusian mantle that is governed
822 by pressure and temperature changes, but not by water content, which may in
823 contrast be relevant for Earth. This remains somewhat speculative, however
824 without coupling our interior evolution model to water and volatile content and
825 their effects on effective viscosity. Several recent models of Venus coupling inter-
826 rior and atmosphere consider transport of water and volatiles from the mantle
827 into the atmosphere upon melt extraction (e.g. Noack et al., 2012; Gillmann and
828 Tackley, 2014). Yet, none of them considers the direct effects of water on viscos-
829 ity though (cf. Richard and Bercovici, 2009) with which it could ultimately be

830 tested whether the more gradual venusian mantle viscosity profile is explained
831 by a different water distribution than in the terrestrial mantle.

832 *4.2. The evolutionary state of Venus' present interior*

833 In all our models volcanic resurfacing is ongoing at present-day as previously
834 reported by the numerical studies of Armann and Tackley (2012) and Gillmann
835 and Tackley (2014). Ongoing very recent resurfacing also seems to be in line
836 with current observational inferences from Venus' surface (Smrekar et al., 2010;
837 Bjonnes et al., 2012). The style of resurfacing on modern Venus may also be
838 via localised plume-triggered subduction as observed in recent laboratory-scale
839 experiments and some of the venusian coronae (Davaille et al., 2017). While
840 our episodic cases do feature some local deformation in the shallow lithosphere
841 also in the stagnant-lid phases between overturns, the stresses are too small to
842 induce such localised subduction and/or coronae formation. This may require a
843 more complex rheology that may include distinct crustal and mantle rheologies
844 and additional mechanisms for crustal and lithospheric weakening (e.g. Gerya,
845 2014).

846 With these limitations aside, resurfacing in our models away from large-scale
847 overturn events happens via melt extraction (magmatic/volcanic recycling).
848 Stagnant-lid models then feature large mean crustal thicknesses of > 100 km
849 well beyond the basalt-eclogite transition depth. As already inferred by Ar-
850 man and Tackley (2012) in 2D models this is not substantially improved when
851 heat-producing elements are more abundant in the basaltic crust (Figure 8) and
852 similarly if Venus' bulk internal heating rate was moderately lower for some rea-
853 son. Such thicknesses are well beyond other independent estimates that mostly
854 come from spectral admittance modelling. For instance, Anderson and Sm-
855 rekar (2006) suggested a global range of crustal thickness from 0 – 90 km and
856 Steinberger et al. (2010) derived a mean value of ~ 60 km based on matching
857 Venus' gravity power-spectrum at $l > 40$, which is likely dominated by crustal
858 contributions. More recently, Wei et al. (2014) used the convection model so-
859 lutions of Huang et al. (2013) to correct for the dynamic contributions that
860 affect long-wavelength topography and geoid and inferred a smaller range of
861 crustal thicknesses on Venus of 28 – 70 km and James et al. (2013) even sug-
862 gested a mean crustal thickness of Venus of only 8 – 25 km. Crustal thickness
863 estimates from spectral admittance modelling are intrinsically non-unique (e.g.
864 Wieczorek, 2007), but all these studies consistently predict thinner crust than
865 inferred from our stagnant-lid models (Table 3). With an upper mantle viscosity
866 about a factor ~ 30 lower than inferred from our best fit model, average crustal
867 thickness may be lower (Armann and Tackley, 2012) and closer to these obser-
868 vational estimates. Indeed, we observe the same trend (case S2 vs. S1), but
869 constraints on numerical resolution currently do not allow us to reduce upper
870 mantle viscosity further in our 3D model. However, we also note that the fit to
871 observed spectral characteristics of gravity and topography starts to degrade for
872 our lowest viscosity case (S1, see Figure 2a-d), so crustal thickness may become
873 more realistic, but the predicted gravity power spectra may not.

874 In line with Armann and Tackley (2012), episodic overturns are the most

875 feasible way to realise crustal thicknesses as inferred above. In contrast to the
876 stagnant-lid models, crustal thickness is self-regulated in episodic models since
877 too thick crust will trigger an overturn and thus reset crustal thickness, poten-
878 tially globally. This way, our models can match above inferences at least at
879 their upper end. We note, that mean crustal thickness still tends to be rather
880 high, which may be linked to the simplifications in the melt extraction model
881 (see section 4.3).

882 Regardless of the absolute value, the growth of crustal thickness between
883 major overturn events seems to occur almost linearly (Figure 8b). For instance,
884 in our preferred model E50, the crust thickens with a rate of ~ 18 km/Gyr since
885 the last overturn. Unfortunately, this rate seems to vary even for the same
886 concentration of radiogenic elements in the mantle depending on previous evo-
887 lution and thus the yield strength (e.g., compare cases E50 and E70 in Figure
888 8b), which is largely unconstrained. Moreover, mean crustal thickness is not
889 reset to zero after the overturn, but to a finite value that typically lies between
890 25–35 km in our set of evolutions. Consequently, inferring the possible cessation
891 time of the last venusian overturn event from present crustal thickness estimates
892 and (linear) back-interpolation of crustal growth rates seems inappropriate at
893 this point.

894 A more obvious way of inferring overturn cessation time would be by using
895 the age distribution of Venus’ surface. In our stagnant-lid models the (upper)
896 mantle stays very hot throughout the entire evolution, which enhances melting
897 and magmatism and thus leads to stronger rates of volcanic resurfacing: this
898 leads to present-day mean surface ages of < 350 Myr (Figure 9). In contrast,
899 the episodic evolutions tend to feature clearly reduced volcanic eruption rates
900 (e.g., Figure 4c). It is thus easier to maintain an older surface, so that mean
901 surface ages of ~ 600 Myr can be generated. Such values are more in line with
902 constraints from the cratering population (McKinnon et al., 1997), although the
903 possibility of a very young surface for Venus has recently been suggested by Bot-
904 tke et al. (2016), who revisited venusian impactor fluxes. The episodic models
905 thus outperform the stagnant-lid models in terms of mean surface age (as for
906 the gravity spectra and crustal thicknesses), so that this diagnostic supports the
907 occurrence of an overturn in the venusian evolution. Stagnant-lid evolutions,
908 on the other hand, seem more feasible in generating a uniform surface age in an
909 absolute sense (see Figure 9). When lateral age variations are put into relation
910 with the respective mean age, however, this observation can vanish and even
911 turn around, that is the episodic evolution can even predict slightly better uni-
912 formity than the stagnant-lid evolution. Nonetheless, our current model does
913 not succeed in predicting uniform age distributions in a strict sense, indepen-
914 dent of the evolution scenario.

915 As a consequence, we put the emphasis on mean age rather than uniformity
916 for this study, also because the degree of uniformity remains under debate for
917 the case of present Venus whose surface age is probably also not strictly uniform
918 (e.g. Nikishin, 1990; Basilevsky and Head, 2002). For example, tesserae terrains
919 may be as old as 1.47 ± 0.46 -times the mean age (Ivanov and Basilevsky, 1993)
920 while some lava flow fields and large volcanoes may be as young as 0.41 ± 0.29 -

921 and 0.23 ± 0.15 -times the mean age, respectively (Price and Suppe, 1994). Re-
922 cently, Kreslavsky et al. (2015) suggested that the average age of young (old)
923 units may be ~ 0.4 (1.2)-times the mean surface age. A detailed comparison of
924 model-predicted surface age distributions with geological constraints needs to
925 be performed in future. This may provide further insight into resurfacing rates
926 and/or the time passed since the latest overturn of Venus' lithosphere.

927 That our current models have difficulty in generating uniform age distribu-
928 tions could be due to spatially heterogeneous magmatic activity as it happens
929 more frequently in hotter regions, for instance the locations of hot upwellings.
930 An uniform surface age would require that volcanic resurfacing is either shut
931 down or happens everywhere at a comparable rate. While our stagnant-lid
932 cases tend to the latter, this scenario seems unlikely for present-day Venus. The
933 strong degradation of the uniform age distribution in our modelling may also
934 be rooted in our simple melting model in which all magmatism is extrusive. In
935 reality, most magmatism will be intrusive and will thus not directly contribute
936 to resurfacing (see section 4.3).

937 At this stage, it remains difficult to decide whether the stagnant-lid or the
938 episodic models generate a more Venus-like age distribution. With on-going
939 magmatism, it can only be said that the presently observed mean surface age
940 is a minimum estimate for the time passed since the latest overturn event: the
941 more volcanic resurfacing has happened after the overturn ceased, the larger is
942 the time difference Δt between cessation time and mean surface age. In our
943 best-fit model (E50), Δt is large (~ 1 Gyr), but this is probably an overesti-
944 mation because we ignore volcanic intrusions as explained above. Nevertheless,
945 a large Δt is in line with our observation that the pattern of mantle plumes
946 requires a long time to recover from the latest overturn and form a pattern
947 that is characteristic of the stagnant-lid scenario (Figures 3 and 7). The small
948 number of observed surface thermal emissivity anomalies (Smrekar et al., 2010)
949 suggests that the plume pattern has readjusted after the overturn already and
950 is representative of the stagnant-lid phase of the evolution. We cannot ulti-
951 mately exclude the possibility that the plume pattern has not (yet) responded
952 substantially to a rather recent overturn event (e.g., see case E60, Figure 7d),
953 but this would probably imply a very young surface in conflict with most age
954 estimates of the venusian surface. Clearly, more future work is required to re-
955 fine the time scale of plume recovery and how it depends on the properties of
956 the lower mantle including the bottom thermal boundary layer. Also, it is not
957 well established that each mantle plume causes a thermal emissivity anomaly
958 or whether anomalies may also be triggered by different processes.

959 The surface gravity spectrum is certainly a more robust constraint than the
960 observed plume pattern, but according to our models it cannot help to further
961 constrain the cessation time of the last overturn since the remnants of large-
962 scale surface recycling vanish quickly after the end of the overturn (~ 150 Myr,
963 Figure 6e). Thus, the present-day spectrum should be clearly representative of
964 a stagnant-lid phase, unless recycled material is somehow kept more efficiently
965 at shallower depth ranges that influence surface gravity more than the CMB re-
966 gion where recycled material accumulates in our models. Armann and Tackley

967 (2012) predicted a somewhat stronger accumulation of basaltic material in the
968 transition zone as we observed here, probably due to details in the density struc-
969 ture of the transition zone (density jumps and Clapeyron slopes of the different
970 phase transitions, depth-dependent thermodynamic parameters and compress-
971 ibility). This may promote density anomalies in this region of the mantle, but
972 the results of Armann and Tackley (2012) (see their Figure 5) suggest that this
973 effect decreases with increasing reference viscosity η_0 , so that the effect should
974 be rather small in our presumably most-representative case of Venus (E50).

975 As a summarising note from our modelling, it seems that model-predicted
976 gravity and topography as well as crustal thickness and mean surface age con-
977 straints are in better agreement with observational inferences when an episodic
978 lid regime with a least one catastrophic overturn is considered. However, the
979 slow recovery of the plume pattern after an overturn may suggest that the cur-
980 rent stagnant-lid phase on Venus is ongoing for quite some time. A new overturn
981 event may occur in future.

982 *4.3. Limitations*

983 We have presented self-consistent models of Venus’ thermochemical man-
984 tle evolution in full 3D spherical geometry including global episodic overturns.
985 This is an advancement from previous attempts to model Venus’ interior. Our
986 approach still has limitations several of which have been discussed above al-
987 ready, for example neglecting mantle compressibility and the depth-dependence
988 of thermodynamical parameters, which may alter the density structure of the
989 mantle. We also assumed the absence of water and volatile cycling and we have
990 not varied the initial condition of our model, although this may not have great
991 influence given the long time scale of evolution and the vigorously convecting
992 mantle.

993 No interaction between Venus’ atmosphere and the interior has been as-
994 sumed, but recently, Gillmann and Tackley (2014) have shown that mantle
995 outgassing can change the composition of the atmosphere, which may lead to
996 changes in Venus’ surface temperature and may ultimately trigger overturn
997 events. This may alter the frequency, style, and duration of overturns and
998 ultimately the thermomagmatic evolution of the whole planet (see e.g. Foley
999 and Driscoll, 2016). In a further step, Gillmann et al. (2016) demonstrated that
1000 this coupled system may also be affected by asteroidal impacts, which erode the
1001 atmosphere and could be another trigger for overturn events.

1002 The modulation of surface temperature by interior-atmosphere coupling may
1003 also impact damage and healing processes in the lithosphere, which could be
1004 important for the initialisation of surface mobilisation and the persistence of
1005 weak zones (e.g. Bercovici and Ricard, 2014). This possibly affects Venus’ evo-
1006 lution particularly if its surface temperature variations are large: Gillmann and
1007 Tackley (2014) present temporal fluctuations of several 100s of K, thus compa-
1008 rable to the difference between Venus and Earth. More generally, our triggering
1009 mechanism for lithospheric overturns, that is when convective stresses overcome
1010 a yield stress, is simplified. This is indicated by the essentially unconstrained
1011 value of the yield stress, which is largely a tuning parameter. Other mechanisms

1012 such as grain size evolution (e.g. Foley and Bercovici, 2014) could be important
1013 and may change the style of surface recycling.

1014 But perhaps the most important simplification in our model is the treatment
1015 of magmatic processes. In particular, we assume that all melt above a critical
1016 depth will trigger extrusive volcanism. However, this is not true for the Earth
1017 and probably for other planetary bodies including Venus, where the majority is
1018 intrusive, although the exact ratio is debated. Intrusive magmatism has recently
1019 been shown to strongly affect crustal and lithospheric dynamics on early-Earth
1020 (Rozel et al., 2017) and it is likely that hot intrusions may also modify the ther-
1021 momechanical state of the venusian lithosphere and thus the planet’s resurfacing
1022 mode (Tackley et al., 2014). These aspects should be considered in future work.

1023 5. Conclusions

1024 We have investigated the thermal, compositional, magmatic and tectonic
1025 evolution of the planet Venus using the mantle convection code StagYY in real-
1026 istic 3D spherical geometry. Our main goal has been to infer Venus present-day
1027 state, in particular its mantle viscosity structure and to infer the evolutionary
1028 path of Venus based on present-day observables. Our results may be synthesised
1029 in the following concluding remarks:

- 1030 1. In our stagnant-lid evolution models, Venus’ observed power spectrum of
1031 surface gravity and its relation to topography is best-matched when sub-
1032 lithospheric mantle viscosity at ~ 200 km depth is $\sim 2 \times 10^{20}$ Pa s and
1033 increases gradually with depth by a factor of ~ 100 to a maximum value
1034 of $\sim 2 \times 10^{22}$ Pa s at around 250 – 300 km above the core-mantle boundary.
1035 A stronger viscosity increase, particularly if caused by a discontinuity in
1036 the transition zone, is unfavourable as it inhibits the strong correlation
1037 of gravity and topography observed for Venus. The lack of such a viscos-
1038 ity increase in the transition zone on Venus may point to different water
1039 contents in the upper mantles of Venus and Earth, where the latter is
1040 more hydrated and thus features lower viscosity. Our most-representative
1041 stagnant-lid models generate a plume pattern in line with thermal emis-
1042 sivity constraints of Venus’ surface, but always lead to too thick basaltic
1043 crust (> 100 km) and tend to feature too young surface age (< 300 Myr).
- 1044 2. Evolutions with a few episodic overturns generate very similar viscosity
1045 structures as in the stagnant-lid mode if the last overturn event has ceased
1046 for a sufficiently long time. In these models, the spectral characteristics
1047 of Venus’ gravity and topography can be matched even better than in the
1048 stagnant-lid models, in particular at the longest wavelength. Such evolu-
1049 tions predict a much reduced crustal thickness ($\sim 40 - 60$ km) in much
1050 better consistency with previous estimates and more reasonable mean sur-
1051 face age (~ 600 Myr), but on the other hand a more complex evolution of
1052 the mantle plume pattern that may need a long time to recover from an
1053 overturn event.

1054 3. Overturn events may mobilise the surface globally for ~ 150 – 200 Myr and
1055 may perturb the predicted gravity power spectra for up to another ~ 150 –
1056 200 Myr after surface mobilisation as ceased. This may provide a minimum
1057 estimate of the cessation of Venus’ latest global overturn event and suggest
1058 that the present venusian mantle should not contain any remnants of this
1059 overturn, perhaps with the exception of the region atop the core mantle
1060 boundary where overturn remnants may reside for much longer time and
1061 perturb the development of a stable plume pattern comparable to the
1062 stagnant-lid evolutions.

1063 If our model observations from 1.-3. hold true, our work favours a venusian
1064 evolution that is currently in the stagnant-lid regime, but has featured at least
1065 one global event of tectonic recycling, which may have ceased a rather long time
1066 ago. Clearly, more observational data from Venus will be necessary in the future
1067 to confirm our suggestions.

1068 Acknowledgements

1069 All authors receive funding from the Norwegian Research Council through
1070 a Centre of Excellence grant to the Centre for Earth Evolution and Dynamics
1071 (CEED, 223272). Further support has been received through CRATER CLOCK
1072 (235058/F20). All computations have been performed on Stallo, a Notur high-
1073 performance computing facility at the University of Tromsø, under project codes
1074 nn9283 and nn9010. The authors gratefully thank Paul J. Tackley for providing
1075 his StagYY code, Nicola Tosi and Stephen Mojzsis for two constructive reviews,
1076 and the editor Oded Aharonson for handling the manuscript.

1077 References

- 1078 Anderson, F., Smrekar, S., 2006. Global mapping of crustal and lithospheric
1079 thickness on Venus. *J. Geophys. Res.* 111, E08006.
- 1080 Armann, M., Tackley, P., 2012. Simulating the thermochemical magmatic and
1081 tectonic evolution of Venus’s mantle and lithosphere: Two-dimensional mod-
1082 els. *Jour. Geophys. Res.* 117, E12003.
- 1083 Basilevsky, A., Head, J., 2002. Venus: Timing and rates of geologic activity.
1084 *Geology* 30, 1015–1018.
- 1085 Benesova, N., Cizkova, H., 2012. Geoid and topography of Venus in various
1086 thermal convection models. *Stud. Geophys. Geod.* 56, 621–629.
- 1087 Bercovici, D., 2003. The generation of plate tectonics from mantle convection.
1088 *Earth Planet. Sci. Lett.* 205, 107–121.
- 1089 Bercovici, D., Ricard, Y., 2014. Plate tectonics, damage and inheritance. *Nature*
1090 508, 513–518.

- 1091 Bjonnes, E., Hansen, V., James, B., Swenson, J., 2012. Equilibrium resurfacing
1092 of Venus: Results from new Monte Carlo modeling and implications for Venus
1093 surface histories. *Icarus* 217, 451–461.
- 1094 Bottke, W., Vokrouhlicky, D., Ghent, B., Mazrouei, S., Robbins, S., Marchi, S.,
1095 2016. On Asteroid Impacts, Crater Scalings Laws, and a Proposed Younger
1096 Surface Age for Venus. *Lunar Planet. Sci. Conf. XLVII, #2016*.
- 1097 Christensen, U., Yuen, D., 1985. Layered Convection Induced by Phase Transi-
1098 tions. *J. Geophys. Res.* 90, 10291–10300.
- 1099 Davaille, A., Smrekar, S.E., Tomlinson, S., 2017. Experimental and observa-
1100 tional evidence for plume-induced subduction on Venus. *Nat. Geosci.* 10,
1101 349–355.
- 1102 Davies, J., 2008. Did a mega-collision dry Venus’ interior? *Earth Planet. Sci.*
1103 *Lett.* 268, 376–383.
- 1104 Driscoll, P., Bercovici, D., 2013. Divergent evolution of Earth and Venus: In-
1105 fluence of degassing, tectonics, and magnetic fields. *Icarus* 226, 1447–1464.
- 1106 Elkins-Tanton, L., Smrekar, S., Hess, P., Parmentier, E., 2007. Volcanism and
1107 volatile recycling on a one-plate planet: Applications to Venus. *J. Geophys.*
1108 *Res.* 112, E04S06.
- 1109 Foley, B., Driscoll, P., 2016. Whole planet coupling between climate, mantle, and
1110 core: Implications for rocky planet evolution. *Geochem. Geophys. Geosyst.*
1111 17, 1885–1914.
- 1112 Foley, B.J., Bercovici, D., 2014. Scaling laws for convection with temperature-
1113 dependent viscosity and grain-damage. *Geophys. J. Int.* 199, 580–603.
- 1114 Gerya, T., 2014. Plume-induced crustal convection: 3D thermomechanical
1115 model and implications for the origin of novae and coronae on Venus. *Earth*
1116 *Planet. Sci. Lett.* 391, 183–192.
- 1117 Ghosh, S., Ohtani, E., Litasov, K., Suzuki, A., Dobson, D., Funakoshi, K., 2013.
1118 Effect of water in depleted mantle on post-spinel transition and implication
1119 for 660km seismic discontinuity. *Earth and Planetary Science Letters* 371,
1120 103 – 111.
- 1121 Gillmann, C., Golabek, G., Tackley, P., 2016. Effect of a single large impact on
1122 the coupled atmosphere-interior evolution of Venus. *Icarus* 268, 295–312.
- 1123 Gillmann, C., Tackley, P., 2014. Atmosphere/mantle coupling and feedbacks on
1124 Venus. *Jour. Geophys. Res.* 119, 1189–1217.
- 1125 Grinspoon, D.H., 1993. Implications of the high D/H ratio for the sources of
1126 water in Venus’ atmosphere. *Nature* 363, 428–431.

- 1127 Hager, B., Clayton, R., Richards, M., Comer, R., Dziewonski, A., 1985. Lower
1128 mantle heterogeneity, dynamic topography and the geoid. *Nature* 313, 541–
1129 545.
- 1130 Herrick, R., 1994. Resurfacing history of Venus. *Geology* 22, 703–706.
- 1131 Herzberg, C., Condie, K., Korenaga, J., 2010. Thermal history of the Earth and
1132 its petrological expression. *Earth Planet. Sci. Lett.* 292, 79–88.
- 1133 Huang, J., Yang, A., Zhong, S., 2013. Constraints of the topography, gravity
1134 and volcanism on Venusian mantle dynamics and generation of plate tectonics.
1135 *Earth Planet. Sci. Lett.* 362, 207–214.
- 1136 Ivanov, M., Basilevsky, A., 1993. Density and morphology of impact craters on
1137 tessera terrain, Venus. *Geophys. Res. Lett.* 20, 2579–2582.
- 1138 James, P., Zuber, M., Phillips, R., 2013. Crustal thickness and support of
1139 topography on Venus. *J. Geophys. Res.* 118, 859–875.
- 1140 Keller, T., Tackley, P., 2009. Towards self-consistent modeling of the martian
1141 dichotomy: The influence of one-ridge convection on crustal thickness distri-
1142 bution. *Icarus* 202, 429–443.
- 1143 Kojitani, H., Inoue, T., Akaogi, M., 2016. Precise measurements of enthalpy
1144 of postspinel transition in Mg₂SiO₄ and application to the phase boundary
1145 calculation. *J. Geophys. Res.* 121, 729–742. 2015JB012211.
- 1146 Kreslavsky, M., Ivanov, M., Head, J., 2015. The resurfacing history of Venus:
1147 Constraints from buffered crater densities. *Icarus* 250, 438–450.
- 1148 McKinnon, W., Zahnle, K., Ivanov, B., Melosh, H., 1997. Venus II. University
1149 of Arizona Press, Tucson, Arizona. chapter Cratering on Venus: Models and
1150 observations. pp. 969–1014.
- 1151 Moresi, L., Solomatov, V., 1998. Mantle convection with a brittle lithosphere:
1152 thoughts on the global tectonic styles of the Earth and Venus. *Geophys. J.*
1153 *Int.* 133, 669–682.
- 1154 Murakami, M., Hirose, K., Yurimoto, H., Nakashima, S., Takafuji, N., 2002.
1155 Water in Earth’s Lower Mantle. *Science* 295, 1885–1887.
- 1156 Nikishin, A., 1990. Tectonics of venus: A review. *Earth Moon Planets* 50/51,
1157 101–125.
- 1158 Noack, L., Breuer, D., Spohn, T., 2012. Coupling the atmosphere with interior
1159 dynamics: Implications for the resurfacing of Venus. *Icarus* 217, 484–498.
- 1160 O’Neill, C., Marchi, S., Zhang, S., Bottke, W., 2017. Impact-driven subduction
1161 on the Hadean Earth. *Nature Geosci.* 10, 793–796.

- 1162 Orth, C., Solomatov, V., 2011. The isostatic stagnant lid approximation and
1163 global variations in the Venusian lithosphere. *Geochem. Geophys. Geosyst.*
1164 12, Q07018.
- 1165 Papuc, A., Davies, G., 2012. Transient mantle layering and the episodic be-
1166 haviour of Venus due to the 'basalt barrier' mechanism. *Icarus* 217, 499–509.
- 1167 Pauer, M., Fleming, K., Cadek, O., 2006. Modeling the dynamic component of
1168 the geoid and topography of Venus. *J. Geophys. Res.* 111, E11012.
- 1169 Price, M., Suppe, J., 1994. Mean age of rifting and volcanism on Venus deduced
1170 from impact crater densities. *Nature* 372, 756–759.
- 1171 Richard, G., Bercovici, D., 2009. Water-induced convection in the Earth's man-
1172 tle transition zone. *J. Geophys. Res.* 114, B01205.
- 1173 Richards, M., Hager, B., 1989. Effects of Lateral Viscosity Variations on Long-
1174 Wavelength Geoid Anomalies and Topography. *J. Geophys. Res.* 94, 10299–
1175 10313.
- 1176 Romeo, I., Turcotte, D., 2010. Resurfacing on Venus. *Plan. Space Sci.* 58,
1177 1374–1380.
- 1178 Rozel, A., Golabek, G., Jain, C., Tackley, P., Gerya, T., 2017. Continental
1179 crust formation on early Earth controlled by intrusive magmatism. *Nature*
1180 545, 332.
- 1181 Schubert, G., Sandwell, D., 1995. A Global Survey of Possible Subduction Sites
1182 on Venus. *Icarus* 117, 173–196.
- 1183 Smrekar, S., Sotin, C., 2012. Constraints on mantle plumes on Venus: Implica-
1184 tions for volatile history. *Icarus* 217, 510–523.
- 1185 Smrekar, S., Stofan, E., Mueller, N., Treiman, A., Elkins-Tanton, E., Helbert,
1186 J., Piccioni, G., Drossart, P., 2010. Recent Hotspot Volcanism on Venus from
1187 VIRTIS Emissivity Data. *Science* 605, 605–608.
- 1188 Solomatov, V., 1995. Scaling of temperature- and stress-dependent viscosity
1189 convection. *Phys. Fluids* 7, 266–274.
- 1190 Steinberger, B., Calderwood, A., 2006. Models of large-scale viscous flow in the
1191 Earth's mantle with constraints from mineral physics and surface observa-
1192 tions. *Geophys. J. Int.* 167, 1461–1481.
- 1193 Steinberger, B., Holme, R., 2002. An explanation for the shape of Earth's
1194 gravity spectrum based on viscous mantle flow models. *Geophys. Res. Lett.*eo
1195 29, 2019.
- 1196 Steinberger, B., Werner, S., Torsvik, T., 2010. Deep versus shallow origin of
1197 gravity anomalies, topography and volcanism on Earth, Venus and Mars.
1198 *Icarus* 207, 564–577.

- 1199 Steinberger, B., Zhao, D., Werner, S., 2015. Interior structure of the Moon:
1200 Constraints from seismic tomography, gravity and topography. *Phys. Earth*
1201 *Planet. Int.* 245, 26–39.
- 1202 Tackley, P., 2008. Modelling compressible mantle convection with large viscosity
1203 contrasts in a three-dimensional spherical shell using the yin-yang grid. *Phys.*
1204 *Earth Planet. Int.* 171, 7–18.
- 1205 Tackley, P., Ammann, M., Brodholt, J., Dobson, D., Valencia, D., 2013. Mantle
1206 dynamics in super-Earths: Post-perovskite rheology and self-regulation of
1207 viscosity. *Icarus* 225, 50–61.
- 1208 Tackley, P., King, S., 2003. Testing the tracer ratio method for modeling active
1209 compositional fields in mantle convection simulations. *Geochem. Geophys.*
1210 *Geosyst.* 4, 2001GC00214.
- 1211 Tackley, P., Lourenco, D., Golabek, G., 2014. Influence of intrusive magma-
1212 tism on Venus’ tectonics and long-term thermo-chemical mantle evolution.
1213 *European Planet. Sci. Congress* 9, 532.
- 1214 Turcotte, D., Schubert, G., 2002. *Geodynamics*. Cambridge University Press,
1215 Cambridge. 2nd edition.
- 1216 Turcotte, D., Willemann, R., Haxby, W., Norberry, J., 1981. Role of Membrane
1217 Stresses in the Support of Planetary Topography. *J. Geophys. Res.* 86, 3951–
1218 3959.
- 1219 Wei, D., Yang, A., Huang, J., 2014. The gravity field and crustal thickness of
1220 Venus. *Science China: Earth Sciences* 57, 2025–2035.
- 1221 Weller, M., Lenardic, A., O’Neill, C., 2015. The effects of internal heating and
1222 large scale climate variations on tectonic bi-stability in terrestrial planets.
1223 *Earth Planet. Sci. Lett.* 420, 85–94.
- 1224 Wiczorek, M., 2007. *Treatise on Geophysics*. Elsevier. volume Volume 10: Plan-
1225 ets and Moons. chapter Gravity and Topography of the Terrestrial Planets.
1226 2 edition.
- 1227 Xie, S., Tackley, P., 2004. Evolution of U-Pb and Sm-Nd systems in numeri-
1228 cal models of mantle convection and plate tectonics. *J. Geophys. Res.* 109,
1229 B11204.
- 1230 Zhang, S., Christensen, U., 1993. Some effects of lateral viscosity variations
1231 on geoid and surface velocities induced by density anomalies in the mantle.
1232 *Geophys. J. Int.* 114, 531–547.
- 1233 Zhong, S., McNamara, A., Tan, E., Moresi, L., Gurnis, M., 2008. A benchmark
1234 study on mantle convection in a 3-D spherical shell using CitcomS. *Geochem.*
1235 *Geophys. Geosyst.* 9, Q10017.